



**CHALMERS**  
UNIVERSITY OF TECHNOLOGY

## **Effect of SO<sub>2</sub> and SO<sub>3</sub> Exposure to Cu-CHA on Surface Nitrate and N<sub>2</sub>O Formation for**

Downloaded from: <https://research.chalmers.se>, 2024-06-29 21:04 UTC

Citation for the original published paper (version of record):

Han, J., Bjerregaard, J., Grönbeck, H. et al (2024). Effect of SO<sub>2</sub> and SO<sub>3</sub> Exposure to Cu-CHA on Surface Nitrate and N<sub>2</sub>O Formation for NH<sub>3</sub>-SCR. ACS ENGINEERING AU, In Press.  
<http://dx.doi.org/10.1021/acsengineeringau.4c00004>

N.B. When citing this work, cite the original published paper.

# Effect of SO<sub>2</sub> and SO<sub>3</sub> Exposure to Cu-CHA on Surface Nitrate and N<sub>2</sub>O Formation for NH<sub>3</sub>-SCR

Joonsoo Han,\* Joachim D. Bjerregaard, Henrik Grönbeck, Derek Creaser, and Louise Olsson\*

Cite This: <https://doi.org/10.1021/acsengineeringau.4c00004>

Read Online

ACCESS |



Metrics &amp; More



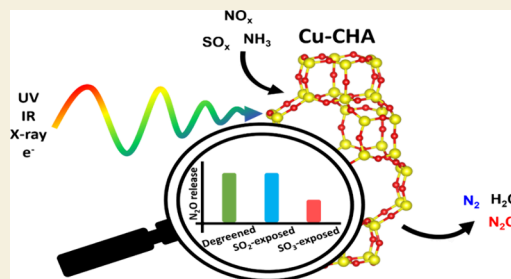
Article Recommendations



Supporting Information

**ABSTRACT:** We report effects of SO<sub>2</sub> and SO<sub>3</sub> exposure on ammonium nitrate (AN) and N<sub>2</sub>O formation in Cu-CHA used for NH<sub>3</sub>-SCR. First-principles calculations and several characterizations (ICP, BET, XRD, UV-vis-DRS) were applied to characterize the Cu-CHA material and speciation of sulfur species. The first-principles calculations demonstrate that the SO<sub>2</sub> exposure results in both (bi)sulfite and (bi)sulfate whereas the SO<sub>3</sub> exposure yields only (bi)sulfate. Furthermore, SO<sub>x</sub> adsorption on framework-bound dicopper species is shown to be favored with respect to adsorption onto framework-bound monocopper species. Temperature-programmed reduction with H<sub>2</sub> shows two clear reduction states and larger sulfur uptake for the SO<sub>3</sub>-exposed Cu-CHA compared to the SO<sub>2</sub>-exposed counterpart. Temperature-programmed desorption of formed ammonium nitrate (AN) highlights a significant decrease in nitrate storage due to sulfur species interacting with copper sites in the form of ammonium/copper (bi)sulfite/sulfate. Especially, highly stable sulfur species from SO<sub>3</sub> exposure influence the NO<sub>2</sub>-SCR chemistry by decreasing the N<sub>2</sub>O selectivity during NH<sub>3</sub>-SCR whereas an increased N<sub>2</sub>O selectivity was observed for the SO<sub>2</sub>-exposed Cu-CHA sample. This study provides fundamental insights into how SO<sub>2</sub> and SO<sub>3</sub> affect the N<sub>2</sub>O formation during ammonium nitrate decomposition in NH<sub>3</sub>-SCR applications, which is a very important topic for practical applications.

**KEYWORDS:** SO<sub>2</sub>/SO<sub>3</sub>-exposure, Cu-CHA, TPD (temperature-programmed desorption), AN (ammonium nitrate), N<sub>2</sub>O



## 1. INTRODUCTION

NH<sub>3</sub>-assisted selective catalytic reduction (SCR) has been extensively applied for NO<sub>x</sub> emission control in stationary and mobile applications (e.g., power plants, automobiles, and ships). Copper-exchanged chabazite (Cu-CHA), composed of a small pore entrance (eight-membered rings, 3.8 × 3.8 Å) and double six-membered rings, has been successfully commercialized in exhaust after treatment systems (EATS) for diesel combustion thanks to its high activity and hydrothermal stability at low and high temperatures, respectively.<sup>1–3</sup> Nitrous oxide (N<sub>2</sub>O) emissions, which may be formed via side reactions during NO<sub>x</sub> reduction, must be regulated because of their ~300 times stronger greenhouse gas potential than carbon dioxide (CO<sub>2</sub>) and depletion of the stratospheric ozone.<sup>4,5</sup> As a result, there is a great deal of interest in understanding the fundamental mechanisms of N<sub>2</sub>O formation during NH<sub>3</sub>-SCR of NO<sub>x</sub> to improve N<sub>2</sub> selectivity and minimize N<sub>2</sub>O emissions.

Utilization of biomass in fuels is indispensable to achieve sustainability goals and reduce fossil fuel usage, resulting in lower fossil carbon dioxide (CO<sub>2</sub>) emissions.<sup>6</sup> However, combustion of petrol, diesel, and biofuels and usage of engine lubricants result in exhaust containing common poisons such as alkali metals, sulfur, phosphorus, and ash, causing contamination of the catalyst and lowering overall deNO<sub>x</sub>

performance in EATS.<sup>7,8</sup> Among the contamination sources, sulfur has been measured to have severe effects on the activity of the SCR catalysts.<sup>9–16</sup> Sulfur is present in the form of sulfur oxides (SO<sub>x</sub>) after combustion of the fuels and originates mainly from the fuel. SO<sub>2</sub>-exposed Cu-CHA shows reduced deNO<sub>x</sub> performance compared to degreened Cu-CHA.<sup>11,12</sup> SO<sub>3</sub>-exposed Cu-CHA, however, shows critically reduced deNO<sub>x</sub> performance and involves larger sulfur storage compared to SO<sub>2</sub>-exposed Cu-CHA.<sup>9,17</sup> Thus, there is a strong demand to find strategies to reduce the effects of sulfur to maintain the catalytic activity during the lifetime of the catalyst.<sup>7</sup> In modern diesel EATS, a diesel oxidation catalyst (DOC) plays an important role to increase the NO<sub>2</sub> content, which promotes NO<sub>x</sub> reduction and passive regeneration of the SCR and diesel particulate filter (DPF), respectively.<sup>18</sup> Unfortunately, SO<sub>2</sub> is mainly oxidized via the DOC and coated DPF, resulting in SO<sub>3</sub> and H<sub>2</sub>SO<sub>4</sub> (formed with water via SO<sub>3</sub>+H<sub>2</sub>O → H<sub>2</sub>SO<sub>4</sub>) in the exhaust gas mixture.<sup>18,19</sup>

**Received:** February 19, 2024

**Revised:** May 17, 2024

**Accepted:** May 20, 2024

Although Europe follows the fuel standard (EN590) limiting the sulfur concentration to a maximum of 10 ppm(w), a substantial amount of sulfur (around 2.5 kg of S) could reach the catalysts in the EATS for heavy-duty applications during its lifespan.<sup>8,20</sup> Periodic regeneration of the DPF (also referred to as active regeneration) can cause temperatures reaching over 650 °C in the filter, which means that also the downstream SCR catalyst is exposed to these high temperatures.<sup>21</sup> During the high temperature, the accumulated surface sulfur species can leave the surface of the oxidation catalysts (DOC/DPF) whereupon the resulting sulfur oxides (SO<sub>2</sub>, SO<sub>3</sub>, and H<sub>2</sub>SO<sub>4</sub>) reach the SCR catalyst. According to the SO<sub>x</sub>-TPD with an EATS configuration (SCR+DOC+DPF+SCR+ASC), the DOC is the main contributor of the SO<sub>3</sub>/H<sub>2</sub>SO<sub>4</sub> generation.<sup>22</sup> With a sulfated SCR catalyst, the adsorbed sulfur species cause CuO formation during the desulfation event. This desulfation event can cause critical loss of the SCR active copper ions to inactive Cu<sub>x</sub>O<sub>y</sub> species without severe zeolite structure deterioration.<sup>23</sup>

NH<sub>3</sub>-SCR reactions undergo different reaction schemes depending on the NO and NO<sub>2</sub> ratio in the exhaust gas mixture.<sup>24,25</sup> With only NO present, the NH<sub>3</sub>-SCR reaction includes O<sub>2</sub> in the reaction stoichiometry and the reaction follows the so-called standard SCR reaction.<sup>24</sup> The SCR catalyst can be exposed to NO<sub>2</sub>, which can be formed via an oxidation catalyst located upstream of the SCR catalyst. When using equimolar NO/NO<sub>2</sub> amounts, the NO<sub>x</sub> reduction rate is enhanced compared to standard SCR, in the so-called fast SCR reaction.<sup>25</sup> However, when the NO<sub>2</sub> content is high, the slow NO<sub>2</sub> SCR reaction occurs, which reduces the reaction rate even when compared to the standard SCR reaction.<sup>25</sup>

Standard SCR: 4NO + 4NH<sub>3</sub> + O<sub>2</sub> → 4N<sub>2</sub> + 6H<sub>2</sub>O

Fast SCR: NO + NO<sub>2</sub> + 2NH<sub>3</sub> → 2N<sub>2</sub> + 3H<sub>2</sub>O

NO<sub>2</sub> SCR (slow SCR): 3NO<sub>2</sub> + 4NH<sub>3</sub> → 3.5N<sub>2</sub> + 6H<sub>2</sub>O

A variety of Cu<sup>+</sup>/Cu<sup>2+</sup> active sites have been identified depending on the temperature and gas composition in Cu-CHA. At a low temperature, H<sub>2</sub>O or NH<sub>3</sub> solvation of the isolated copper sites causes framework-detached mobile Cu species such as Cu<sup>2+</sup>(H<sub>2</sub>O)<sub>x</sub>, Cu<sup>2+</sup>(OH)(H<sub>2</sub>O)<sub>x</sub>, Cu<sub>2</sub><sup>2+</sup>O<sub>2</sub>(NH<sub>3</sub>)<sub>4</sub>, and Cu<sup>+</sup>(NH<sub>3</sub>)<sub>2</sub>.<sup>26</sup> At a high temperature, H<sub>2</sub>O or NH<sub>3</sub> desorption from these mobile Cu-monomer or Cu-dimer species produces framework-bound Cu-monomer (ZCu, ZCu(OH), Z<sub>2</sub>Cu)<sup>26–29</sup> and oxygen- or hydrogen-containing dimer (Z<sub>2</sub>Cu<sub>2</sub>O, Z<sub>2</sub>Cu<sub>2</sub>O<sub>2</sub>, Z<sub>2</sub>Cu<sub>2</sub>O<sub>x</sub>H<sub>y</sub>) species.<sup>27,30–32</sup> The Z denotes a negatively charged framework, and its subscription represents the number of the site. However, under standard SCR conditions at low temperatures (below 250 °C) in the presence of ammonia, the copper species are mobile and the NH<sub>3</sub>-solvated copper dimers ([Cu<sub>2</sub>(NH<sub>3</sub>)<sub>4</sub>O<sub>2</sub>]<sup>2+</sup>) and monomers ([Cu(NH<sub>3</sub>)<sub>2</sub>]<sup>+</sup>) are considered to be key intermediates in the SCR cycle.<sup>2,24,26,33</sup>

Bimodal N<sub>2</sub>O release is measured with a peak at low (below 300 °C) and high (above 300 °C) temperatures during exposure of Cu-CHA in standard SCR conditions.<sup>34–36</sup> According to the standard SCR mechanism at low temperatures, recent experimental studies have shown that N<sub>2</sub>O is only formed in the reduction half cycle (RHC) during the catalytic turnover of the standard SCR cycle.<sup>37</sup> Ab initio calculations describing H<sub>2</sub>NNO decomposition over [Cu<sub>2</sub>(NH<sub>3</sub>)<sub>4</sub>OOH]<sup>2+</sup> complexes explain not only N<sub>2</sub>O formation during the RHC but also the trend of increasing N<sub>2</sub>O formation as a function of Cu content.<sup>36</sup> Low NO oxidation rates compared to NH<sub>3</sub>-SCR rates on Cu-CHA

have been reported by Paolucci et al.,<sup>28</sup> suggesting that NO oxidation is irrelevant to the standard SCR at low temperatures. In addition, the N<sub>2</sub>O formation rate is an order of magnitude higher than the NO<sub>2</sub> formation rate.<sup>37</sup> A pathway where N<sub>2</sub>O is formed via ammonium nitrate (AN) is, thus, not likely to contribute to the N<sub>2</sub>O formation during low-temperature standard SCR. In contrast to the standard SCR, the extent of N<sub>2</sub>O formation is significantly increased when the NO<sub>2</sub> fraction is increased in the gas mixture<sup>5</sup> and the 2+ oxidation state of Cu ions is predominantly observed from in situ XAS over Cu-CHA under fast and NO<sub>2</sub> SCR conditions,<sup>38,39</sup> suggesting that different reaction schemes are involved with respect to the fast and NO<sub>2</sub> SCR conditions. Kubota et al.<sup>40</sup> and Liu et al.<sup>41</sup> demonstrated that AN is an intermediate species for N<sub>2</sub>O under fast/NO<sub>2</sub> SCR conditions. Liu et al.<sup>41</sup> proposed that the fast SCR follows a dual-site mechanism where derived intermediate species (HONO and H<sub>2</sub>NNO) are decomposed at Brønsted sites in a similar manner as the standard SCR scheme suggested by Chen et al.<sup>42</sup> Han et al.<sup>5</sup> proposed that the CHA structure is favorable to form surface nitrates due to promotion of the NO<sub>2</sub> disproportionation within the CHA cage compared to the MFI and BEA structures, and thereby more AN is observed in the CHA structure, followed by MFI and BEA.

After SO<sub>2</sub> exposure, only small or negligible amounts of stored sulfur has been observed in H forms of zeolites upon sulfur exposure,<sup>43–45</sup> indicating that SO<sub>2</sub> storage mainly requires the presence of Cu ions. Physical and chemical poisoning is reported as the sulfur deactivation mechanism in Cu zeolites. SO<sub>2</sub> and NH<sub>3</sub> exposure to Cu-CHA shows decreasing micropore volume with increasing S content, suggesting that pore blocking occurs by ammonia interacting with derived sulfur species.<sup>46</sup> In comparison, only SO<sub>2</sub> exposure shows no considerable micropore volume decrease with S content.<sup>46</sup> Temperature-programmed desorption (TPD) tests with an SO<sub>2</sub>+SCR gas composition gives bimodal SO<sub>2</sub> peaks at low (~400 °C) and high (↑600 °C) temperatures where ammonium sulfate and Cu sulfate are associated, respectively.<sup>10,45,47–49</sup> After regeneration, ammonium sulfate is decomposed and thus it causes a reversible deactivation.<sup>9,47</sup> However, chemically interacting sulfur species at Cu sites (i.e., ZCuHSO<sub>4</sub>) or Al sites (i.e., Al<sub>2</sub>(SO<sub>4</sub>)<sub>3</sub>) are not fully regenerated and these derived sulfur species are highly stable.<sup>9,50</sup> Furthermore, a fairly high temperature (over 700 °C) is necessary to fully desulfate these highly stable sulfur species over Cu-CHA.<sup>9,50</sup> A highly thermal regeneration event can result in a hydrothermal aging (HTA) effect that converts the Cu ions to inactive Cu<sub>x</sub>O<sub>y</sub> and CuAlO<sub>x</sub> species as well as CHA structure degradation.<sup>51</sup> Therefore, high-temperature regeneration can result in irreversible thermal deactivation.

The current mechanistic understanding of the deactivation of SCR catalysts resulting from sulfur is mainly focused on SO<sub>2</sub> exposure of Cu-CHA. There is a strong consensus that SO<sub>2</sub> readily interacts with ZCuOH and that the interaction with Z<sub>2</sub>Cu is weaker.<sup>45,48,52–54</sup> In situ XAS shows that SO<sub>2</sub> interaction with Cu ions, especially NH<sub>3</sub>-solvated mobile Cu dimers ([Cu<sub>2</sub>(NH<sub>3</sub>)<sub>4</sub>O<sub>2</sub>]<sup>2+</sup>), is particularly sensitive to SO<sub>2</sub> as compared to other-state Cu ions such as framework-interacting Cu<sup>+</sup>/Cu<sup>2+</sup> (ZCu/Z<sub>2</sub>Cu) or NH<sub>3</sub>-solvated Cu monomers ([Cu(NH<sub>3</sub>)<sub>2</sub>]<sup>+</sup>).<sup>55</sup> Another XAS study shows that SO<sub>3</sub> exposure does not change the local structure of Cu sites within the zeolite framework (i.e., Cu–O coordination number and the Cu–Cu distance, etc.), indicating that Cu sites remain

highly dispersed after sulfation as well as following desulfation.<sup>56</sup> First-principles calculations performed by Bjerregaard et al.<sup>57</sup> agree with the experimental observations and suggest that the standard SCR deactivation at low temperatures is due to hindered interstage diffusion by ammonium (bi)sulfate species. Thereby, the pairing of Cu-monomer complexes ( $[\text{Cu}(\text{NH}_3)_2]^+$ ) via  $\text{O}_2$  activation is hindered, which is a key intermediate step of the oxidation half cycle (OHC) during standard SCR at low temperatures.<sup>34</sup> The mechanism proposed by Bjerregaard et al.<sup>57</sup> rationalizes the experimental findings, where the NO conversion and the  $\text{N}_2\text{O}$  formation are reduced upon  $\text{SO}_2$  exposure of Cu-CHA during the standard SCR at low temperature.<sup>12,58,59</sup> Mesilov et al.<sup>12</sup> reported that NO<sub>x</sub> conversion and  $\text{N}_2\text{O}$  selectivity are decreased for the  $\text{SO}_2$ -exposed Cu-CHA (Si/Al  $\approx$  7, 3 wt % Cu) during the standard, fast, and  $\text{NO}_2$  SCR reactions. After regeneration, the NO<sub>x</sub> conversion and  $\text{N}_2\text{O}$  selectivity were not fully regenerated for the three overall SCR reactions but the  $\text{N}_2\text{O}$  selectivity was noticeably increased for the  $\text{NO}_2$  SCR compared to the degreened state. A comparative study between the Cu-CHA aged in EATS (270,000–710,000 miles) and HTA+SO<sub>x</sub>-treated Cu-CHA suggests that sulfur species assists CuO formation without a clear structural damage during desulfation.<sup>23</sup> In contrast to the  $\text{SO}_2$  exposure,  $\text{SO}_3$  exposure to Cu-CHA results in larger sulfur uptake and more severe irreversible deactivation.<sup>9</sup>

For industrial applications, understanding the fundamentals of SO<sub>x</sub> chemistry in Cu-CHA as part of an  $\text{NH}_3$  SCR system is critically important to establish an effective desulfation strategy that maintains catalytic activity throughout the usage lifetime of the SCR catalyst. Limited studies are reported with respect to the  $\text{SO}_3$  exposure compared to the  $\text{SO}_2$  exposure effects on Cu-CHA in terms of its deNO<sub>x</sub> performance and  $\text{N}_2\text{O}$  release. There are some studies that have reported the  $\text{SO}_2$  exposure effect on the  $\text{N}_2\text{O}$  formation.<sup>12,37,58,60</sup> However, to the best of our knowledge, there is no comparative study of the evaluation of the AN and  $\text{N}_2\text{O}$  formation for the  $\text{SO}_2$ - and  $\text{SO}_3$ -exposed Cu-CHA, which is the objective of the current study.

## 2. EXPERIMENTAL AND COMPUTATIONAL METHODS

### 2.1. Catalyst Synthesis and Monolith Sample Preparation

Copper-exchanged SSZ-13 (CHA) was prepared by following the hydrothermal synthesis method to acquire a Si to Al molar ratio of  $\approx$ 15 and ca. 1 wt % Cu. Specifically, 1 wt % Cu was set to favor the exclusive presence of ion-exchanged Cu ions inside CHA cage and avoid possible formation of CuO particles. The acquired Cu/SSZ-13 powders were washcoated on honeycomb monolith substrates (cordierite, 400 cpsi, 15 mm  $\times$  20 mm). The specific synthesis and washcoating procedure are described in the Supporting Information (S1. Catalyst synthesis and monolith preparation). The resulting fresh Cu/SSZ-13 powder and monoliths were degreened under standard SCR conditions (400 ppm of  $\text{NH}_3/\text{NO} + 10\% \text{O}_2 + 5\% \text{H}_2\text{O} + \text{Ar}$  as a balance) at 750 °C for 5 h prior to powder sample characterizations and experiments in a synthetic gas bench reactor.

### 2.2. Synthetic Gas Bench (SGB) Reactor Setup

An SGB reactor was used to perform degreening of fresh catalyst powders, SO<sub>x</sub> treatment, and AN temperature-programmed desorption (AN-TPD). Mass flow controllers (MFCs, Bronkhorst) and a controlled evaporator and mixing (CEM, Bronkhorst) system were equipped to provide the required gases ( $\text{Ar}$ ,  $\text{O}_2$ ,  $\text{NH}_3$ ,  $\text{NO}$ ,  $\text{NO}_2$ ,  $\text{N}_2\text{O}$ ,  $\text{N}_2$ ,  $\text{H}_2\text{O}$ , and  $\text{SO}_2$ ). The gas lines were carefully insulated and heated to 191 °C to avoid water condensation and deposition of solids such as AN. Ar was used as an inert balance for all the experiments, and the

total flow was 1.2 NL·min<sup>-1</sup>. The required gas mixture was fed to a horizontal quartz tube (inner diameter: 16 mm). The horizontal quartz tube was wrapped with a heating coil and insulated to heat up and control the reactor temperature. The prepared sample was located inside the quartz tube during the pretreatment and experiments.

### 2.3. $\text{SO}_2$ and $\text{SO}_3$ Exposure to Degreened Cu-CHA

The prepared monoliths were pretreated in the SGB reactor with  $\text{SO}_2$  and a  $\text{SO}_2+\text{SO}_3$  mixture, which will be referred to as  $\text{SO}_2$  and  $\text{SO}_3$  exposure treatments. First, the monolith was degreened under standard SCR conditions (400 ppm of  $\text{NH}_3$ , 400 ppm of  $\text{NO}$ , 10%  $\text{O}_2$ , and 5%  $\text{H}_2\text{O}$ ) at 750 °C for 5 h, following the  $\text{SO}_2$  or  $\text{SO}_3$  treatment sequence, consisting of the following steps: first step: 30 ppm of  $\text{SO}_2 +$  base feed (10%  $\text{O}_2 + 5\% \text{H}_2\text{O} + \text{Ar}$ ) for 1 h; second step: 400 ppm of  $\text{NH}_3 +$  base feed for 2 h; third step: 30 ppm of  $\text{SO}_2 +$  base feed for 1 h. The reason for applying the ammonia in a separate step between the sulfur steps and not simultaneously with SO<sub>x</sub> is that feeding  $\text{SO}_3$  and  $\text{NH}_3$  simultaneously causes large ammonium sulfate deposits in the reactor, which could block the lines, even when heating the lines thoroughly. For the  $\text{SO}_2+\text{SO}_3$  treatment, an external device connected upstream from the SGB reactor was used to generate  $\text{SO}_3$ . Pt/ $\text{Al}_2\text{O}_3$  (7.5 wt % Pt) was used as an oxidation catalyst in the  $\text{SO}_3$  generator. The specific procedures are described in the Supporting Information (S2.  $\text{SO}_3$  calibration and  $\text{SO}_3$ -exposure of degreened monoliths). This provided the capability to introduce 24 ppm of  $\text{SO}_3 + 6$  ppm of  $\text{SO}_2$  with base feed to the monolith instead of 30 ppm of  $\text{SO}_2$ , as illustrated in Figure S2. Meanwhile, the temperature of the monolith was maintained at 400 °C during the SO<sub>x</sub> treatment to mimic the SO<sub>x</sub> exposure environment to the SCR catalyst during periodic regeneration of the DPF. Note that for simplification from here on, the  $\text{SO}_2$  and  $\text{SO}_2+\text{SO}_3$  treatments shall be referred to as  $\text{SO}_2$  and  $\text{SO}_3$  exposure, respectively.

### 2.4. Catalyst Characterization

Elemental analysis was performed with powder forms of the degreened and  $\text{SO}_2$ - and  $\text{SO}_3$ -exposed samples. The SO<sub>x</sub>-exposed samples' washcoats were carefully scraped from the  $\text{SO}_2$ - and  $\text{SO}_3$ -exposed monoliths. Afterward, the SO<sub>x</sub>-exposed washcoat samples were used for the characterizations. However, for diffuse reflectance infrared Fourier transform spectroscopy (ICP) and diffuse reflectance infrared Fourier transform spectroscopy (DRIFTS) results of the sulfated samples, crushed monoliths were used.

**2.4.1. Catalyst Powder Sample Characterization.** Elemental compositions of the fresh catalyst powders were analyzed using inductively coupled plasma sector field mass spectrometry (ICP-SFMS) at ALS Scandinavia AB. For sulfated samples, washcoated sulfated monoliths were crushed well into a fine powder form to acquire the S/Cu molar ratio; afterward, the sulfur content of the sulfated samples was determined.

Powder X-ray diffraction (XRD) was performed with degreened and  $\text{SO}_2$ - and  $\text{SO}_3$ -exposed samples to confirm the crystalline structure of CHA. A Siemens DS000 diffractometer operating at 40 kV, using the  $K\alpha_1$  radiation of a Cu anode as X-ray source ( $\lambda = 1.54060 \text{ \AA}$ ), was used for measuring the X-ray diffractogram from the powder samples.

$\text{N}_2$  physisorption was performed to measure specific surface area using the Brunauer–Emmett–Teller (BET) method of the degreened catalyst powder. A Micromeritics TriStar 3000 instrument was used to measure the  $\text{N}_2$  adsorption/desorption isotherms at 77 K. Prior to the measurements, the H and Cu forms of the degreened catalyst powders were degassed at 225 °C for 8 h.

UV–visible diffuse reflectance spectroscopy (UV–vis-DRS) was performed to investigate the formation of copper and ammonium sulfate/sulfate species. A Lambda 365 (PerkinElmer) double-beam UV visible spectrophotometer was used to acquire the UV spectrum. The system is composed of two different lamps (D2 and tungsten lamp) for measurement within the UV and visible-light regions. The lamp change occurred at 380 nm during the measurement. The light is split into two beams before it interacts with the sample. One of the beams is used as a reference, and the other beam reaches the sample.

Two detectors (photodiodes) measured the light intensity, which came from the reference and sample beams simultaneously. Detector and reflectance sphere (sphere diameter: 60 mm, sample port aperture: 12.5 mm, sphere coating: Barium sulfate) modules were installed. Thereafter, a light trapper and a white standard were used for the calibration of UV intensity. Finally, the prepared catalyst powder was transferred to a powder cell for measuring the powder sample. The sample was scanned from 1100 to 210 at 5 nm slit width and 480 nm·min<sup>-1</sup> scanning speed.

**2.4.2. H<sub>2</sub> Temperature-Programmed Reduction (H<sub>2</sub>-TPR).** H<sub>2</sub>-TPR was carried out with a differential scanning calorimeter (Sensys DSC calorimeter from Setaram) to investigate the reduction properties of the degreened and SO<sub>2</sub>- and SO<sub>3</sub>-exposed catalyst powders. The powders were carefully sieved to 180–250 μm fraction. Degreened (ca. 50 mg) or SO<sub>x</sub>-exposed (ca. 26 mg) samples were loaded into a quartz tube located inside the DSC, and 0.2% H<sub>2</sub>/Ar was continuously fed at 20 N mL·min<sup>-1</sup> during the experiment. Initially, the temperature was set at 25 °C for 20 min and then was ramped up to 800 °C at 10 °C·min<sup>-1</sup>; thereafter, 800 °C was maintained for 20 min. Note that there was no pretreatment done prior to H<sub>2</sub>-TPR. In the meantime, the outlet gases from the DSC were monitored with mass spectrometry (Hidden HPR-20 QUI MS) for H<sub>2</sub> (*m/e* = 2), NH<sub>3</sub> (15), H<sub>2</sub>O (18), Ar (20), O<sub>2</sub> (32), H<sub>2</sub>S (34), SO<sub>2</sub> (64), SO<sub>3</sub> (80), and H<sub>2</sub>SO<sub>4</sub> (98).

**2.4.3. Ammonium Nitrate Temperature-Programmed Desorption (AN-TPD).** AN-TPD was performed to investigate the effect of SO<sub>2</sub> and SO<sub>3</sub> on AN and N<sub>2</sub>O formation in the SGB reactor. 200 ppm of NH<sub>3</sub>/NO<sub>2</sub> + 5% H<sub>2</sub>O + Ar was fed to the monolith for 90 min at 150 °C, followed by purging with 5% H<sub>2</sub>O+Ar for 90 min. Thereafter, the temperature was increased to 550 °C at 10 °C·min<sup>-1</sup> and then maintained at 550 °C for 20 min while the monolith was exposed to 5% H<sub>2</sub>O+Ar. Note that no pretreatment was done prior to AN-TPD for the SO<sub>2</sub>- and SO<sub>3</sub>-exposed samples, to avoid the removal of sulfur species. However, the degreened sample was pretreated before AN-TPD. An empty-tube test was done prior to AN-TPD to check for possible AN formation. The test result showed no N<sub>2</sub>O formation during temperature ramping, indicating that the system was sufficiently insulated to prevent any significant AN formation during the NH<sub>3</sub>+NO<sub>2</sub> feed to the SGB. Meanwhile, the N<sub>2</sub> (*m/e* = 28) signal evolved while 200 ppm of NO<sub>2</sub>/NH<sub>3</sub> was fed, suggesting that NO<sub>2</sub>-SCR occurred during ionization within MS.

**2.4.4. In Situ DRIFTS Measurements.** In situ DRIFTS was performed to monitor surface nitrite/nitrate and NH<sub>3</sub> interaction with the prepared samples (i.e., degreened and SO<sub>2</sub>- and SO<sub>3</sub>-exposed samples). A VERTEX 70 FTIR spectrometer (Bruker) equipped with a liquid N<sub>2</sub>-cooled mercury cadmium telluride (MCT) detector was used to acquire the IR spectra. Degreened powder samples or crushed SO<sub>x</sub>-exposed monoliths were loaded into a sample cup inside a reaction cell. A KBr bed was set on the bottom of the sample cup, and then the remaining volume of the sample cup was filled with sample. The reaction cell was covered well and mounted with a Ca<sub>2</sub>F window. A thermocouple was installed at the center of a sample bed to monitor the sample bed temperature during the measurement. The temperature of the sample bed was controlled at 150 °C with a PID regulator (Eurotherm 2416), and MFCs (Bronkhorst Hi-Tech) were set to supply the required gas mixture to the reaction cell. 1% H<sub>2</sub>O + Ar was fed as base feed throughout the measurement. The required gases were fed in the following steps: (1) heating to 150 °C in base feed only and (2) 400 ppm of NO<sub>2</sub> + base feed for 1.5 h. Meanwhile, DRIFTS spectra were measured (accumulation of 60 scans, resolution of 4 cm<sup>-1</sup>) over time under 100 N mL·min<sup>-1</sup> of total flow. The outlet gas leaving the reaction cell was continuously monitored with mass spectrometry (Hidden HPR-20 QUI MS). Note that the reported temperature in the DRIFTS test was monitored by a thermocouple located at the center of the sample bed. However, the heating plate located under the sample cup was set at 242 °C. Thus, a temperature gradient resulting from thermal radiation was present and expected.

**2.4.5. First-Principles Calculations.** Spin-polarized density functional theory (DFT) calculations were performed using the Vienna Ab initio Simulation Package (VASP).<sup>61,62</sup> The Kohn–Sham

orbitals were expanded with plane waves with a 480 eV cutoff value, and the interaction between the core and valence electrons was described by the projector augmented wave (PAW)<sup>63,64</sup> method. The valence electrons treated for each atom were Cu(11), Si(4), S(6), Al(3), O(6), and H(1). The k-point sampling was restricted to the gamma point. The Perdew–Burke–Ernzerhof (PBE)<sup>65</sup> functional was used to describe the exchange–correlation effects. To account for van der Waals interactions, the Grimme 3D approach<sup>66</sup> was applied and a Hubbard *U*-term was used to describe the localized Cu 3d electrons, with the *U* value set to 6 eV.

The convergence criteria for the self-consistent field (SCF) loop was set to 10<sup>-5</sup> eV, and structures were considered to be at a minimum if the norm of all forces was less than 0.02 eV/Å. The transition states were located using the Climbing Image Nudged Elastic Band (CI-NEB) approach<sup>67,68</sup> and was confirmed by a single imaginary frequency. Vibrational analysis was performed using the finite difference method. To sample low energy configurations, ab initio molecular dynamics (AIMD) simulations were carried out at 300 K using a Nosé–Hoover thermostat in the NVT ensemble.<sup>69,70</sup> Several structures along the trajectories were extracted and relaxed to determine the low-energy structures. Bader charge analysis was performed using the implementation from the Henkelman group.<sup>71,72</sup> To describe the CHA cage, a hexagonal unit cell containing 36 Si and 72 O was used with the experimental lattice constants (13.8026 Å, 13.8026 Å, 15.0753 Å). For each Cu ion introduced into the unit cell, one Si atom was replaced by one Al atom for charge compensation.

## 3. RESULTS

### 3.1. First-Principles Calculation on SO<sub>x</sub> Adsorption over Cu Sites

Two experimentally observed resting states of the Cu<sup>2+</sup> ions in CHA are Z<sub>2</sub>Cu and ZCuOH.<sup>26,73</sup> Depending on the sample composition and pretreatment, other Cu<sup>2+</sup> sites may form and it is important to consider which Cu sites may be present under the conditions investigated. In our study, the samples have been exposed to SO<sub>x</sub> at 400 °C in the presence of O<sub>2</sub> and H<sub>2</sub>O. At 400 °C, Cu<sup>2+</sup> is mainly bound to the framework and we would therefore expect to have both Z<sub>2</sub>Cu and ZCuOH present. In addition, the presence of O<sub>2</sub> could lead to the formation of Cu dimers as copper ions can possibly migrate, forming a pair of Cu<sup>2+</sup> ions, which can adsorb O<sub>2</sub> forming Z<sub>2</sub>CuO<sub>2</sub>Cu complexes.<sup>74</sup> Other similar dimer sites have been proposed such as Z<sub>2</sub>Cu–O–Cu and Z<sub>2</sub>CuO<sub>2</sub>H<sub>2</sub>Cu.<sup>30,75,76</sup> The Cu sites that will be investigated in the computational study are Z<sub>2</sub>Cu, ZCuOH, and Z<sub>2</sub>CuO<sub>2</sub>Cu.

To explore the effect of SO<sub>2</sub> and SO<sub>3</sub>, we calculated reaction pathways for the formation of CuHSO<sub>3</sub> and CuHSO<sub>4</sub> on Z<sub>2</sub>Cu, ZCuOH, and Z<sub>2</sub>CuO<sub>2</sub>Cu. The reaction of SO<sub>2</sub> on Z<sub>2</sub>Cu and ZCuOH has previously been studied using DFT calculations by Jangjou et al.,<sup>45</sup> and they found that the addition of SO<sub>2</sub> results in the formation of more stable CuHSO<sub>3</sub> complexes on ZCuOH than on Z<sub>2</sub>Cu. In addition, they found that the formation of CuHSO<sub>3</sub> exhibited a lower activation barrier when it was formed on ZCuOH.<sup>45</sup> Furthermore, the stability of CuHSO<sub>x</sub> complexes from the reaction of SO<sub>2</sub> and SO<sub>3</sub> with ZCuOH has been considered with DFT calculations<sup>13</sup> and it was found that adsorption of SO<sub>3</sub> gives rise to more stable complexes than SO<sub>2</sub> adsorption. However, the understanding of the reaction of SO<sub>3</sub> with ZCuOH and Z<sub>2</sub>Cu and the role of Z<sub>2</sub>CuO<sub>2</sub>Cu upon sulfur exposure is currently limited. Herein, we investigate the reaction pathway for the combinations of SO<sub>2</sub> and SO<sub>3</sub> on Z<sub>2</sub>Cu, ZCuOH, and Z<sub>2</sub>CuO<sub>2</sub>Cu, which are Cu sites expected to be present during the first sulfation step in our study.

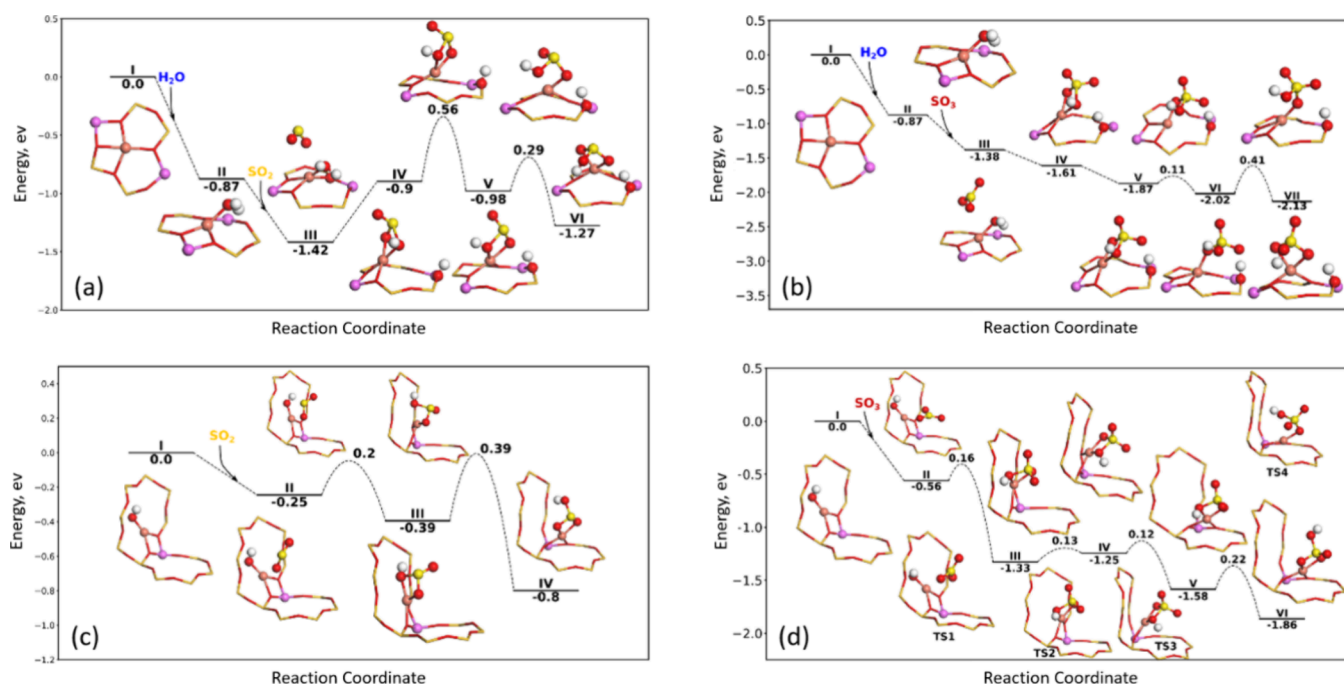


**Figure 1.** Energy landscapes for  $\text{SO}_2$  and  $\text{SO}_3$  adsorption onto  $\text{Z}_2\text{Cu}$  (a, b) and  $\text{ZCuOH}$  (c, d) and the subsequent formation of  $\text{CuHSO}_x$  complexes. Atomic color codes: H (white), N (blue), O (red), Al (pink), Si (dark yellow sticks), S (yellow), and Cu (bronze).

The reaction of  $\text{SO}_2$  and  $\text{SO}_3$  with  $\text{Z}_2\text{Cu}$  is calculated in the presence of a single adsorbed  $\text{H}_2\text{O}$  molecule. If there is no adsorbed  $\text{H}_2\text{O}$  molecule on  $\text{Z}_2\text{Cu}$ , it was not possible to form any stable structures with  $\text{SO}_2$  and  $\text{SO}_3$ , which is in agreement with a previous observation by Jangjou et al.<sup>45</sup> for  $\text{SO}_2$  reacting with  $\text{Z}_2\text{Cu}$ . For the reaction of  $\text{SO}_2$  with  $\text{Z}_2\text{Cu}$  (Figure 1a),  $\text{H}_2\text{O}$  adsorbs on the Cu ion with a Cu–O bond length of 1.95 Å and an adsorption energy of 0.87 eV (I → II). The introduction of  $\text{SO}_2$  in the zeolite cage is preferred by 0.55 eV, compared to  $\text{SO}_2$  in the gas phase; however, we do not find any bond to the Cu ion (II → III). Instead, the oxygen in  $\text{SO}_2$  coordinates to Cu with a bond length of 2.49 Å. The first step in the reaction of  $\text{SO}_2$  with  $\text{Z}_2\text{Cu}$ – $\text{H}_2\text{O}$  results in the cleavage of the H–OH bond, forming a  $\text{CuHSO}_3$  complex and a Brønsted acid site (BAS), which is endothermic by 0.52 eV (III → IV). From a Bader charge analysis, sulfur in  $\text{CuHSO}_3$  is in a +4 oxidation state, as is the case for the gas-phase  $\text{SO}_2$ . In IV, sulfur binds through an OH group, which is not the preferred configuration. In structure IV, the –OH group in  $\text{CuHSO}_3$  coordinates with the BAS with an SO–HBAS bond length of 3.73 Å. In the next step (IV → V), the  $\text{CuHSO}_3$  complex is rotated. The barrier for the rotation (0.56 eV) is related to the change in which group is coordinating with the Brønsted site. In structure V, an oxygen from  $\text{CuHSO}_3$  is coordinating with the Brønsted site resulting in a slight stabilization. The last step is the breakage of the SOH–Cu bond and formation of a SO–Cu bond (V → VI), which is 0.29 eV lower in energy. The final structure is 0.15 eV higher in energy compared to the case with  $\text{SO}_2$  physisorbed in the cage (structure III). Moreover, as the formation of structure Cu is associated with a high activation barrier, we conclude that the reaction of  $\text{SO}_2$  with  $\text{Z}_2\text{Cu}$  is not favorable.

$\text{SO}_3$  can also react with  $\text{Z}_2\text{Cu}$ , as shown in Figure 1b. The first step is also, in this case, the adsorption of  $\text{H}_2\text{O}$  (I → II). Introducing  $\text{SO}_3$  into the cage does not result in adsorption; instead,  $\text{SO}_3$  is physisorbed (exothermic by 0.51 eV) with one

oxygen coordinated to Cu with a bond length of 3.3 Å (II → III).  $\text{SO}_3$  can react with  $\text{H}_2\text{O}$ , splitting the O–H bond in  $\text{H}_2\text{O}$  and forming a  $\text{CuHSO}_4$  complex and a Brønsted site (III → IV). From Bader charge analysis, sulfur remains in a +6 oxidation state, as is the case for the gas-phase  $\text{SO}_3$ . In structure IV, the OH group in  $\text{CuHSO}_4$  is coordinating with HBAS. The next step (IV → V) is related to a change of coordination, resulting in the oxygen of  $\text{CuHSO}_4$  coordinating to HBAS with a bond length of 1.64 Å. The scission of the SOH–Cu bond has a small barrier of 0.11 eV and is preferred by 0.15 eV (V → VI). The last step is the rotation of  $\text{CuHSO}_4$ , resulting in the formation of a second SO–Cu bond (VI → VII). This step has a barrier of 0.41 eV and is exothermic by 0.11 eV. The final structure (VIII) is 0.75 eV more stable compared to the case of having physisorbed  $\text{SO}_3$  (structure III). When comparing the reaction of  $\text{SO}_2$  and  $\text{SO}_3$  with  $\text{Z}_2\text{Cu}$ , it becomes clear that  $\text{SO}_3$  forms  $\text{ZCuHSO}_4$  complexes that are more stable (0.86 eV in difference) than  $\text{ZCuHSO}_3$  complexes formed by the reaction with  $\text{SO}_2$ . The highest activation barrier for formation of  $\text{ZCuHSO}_4$  is 0.41 eV (VI → VII), while the effective barrier is 1.46 eV (III → V) for formation of  $\text{ZCuHSO}_3$ . This suggests that  $\text{SO}_3$  may result in more severe deactivation than  $\text{SO}_2$ . The higher stability of sulfur species in Cu-CHA with the oxidation state of +6 is in agreement with previous DFT studies.<sup>77</sup>

The reaction of  $\text{SO}_x$  with  $\text{ZCuOH}$  can proceed in the absence of  $\text{H}_2\text{O}$ . The introduction of  $\text{SO}_2$  into the CHA cage is preferred by 0.25 eV (I → II, Figure 1c). Next,  $\text{SO}_2$  can react with  $\text{ZCuOH}$  forming a  $\text{CuHSO}_3$  complex that is preferred by 0.14 eV and associated with a small barrier of 0.2 eV (II → III). The last step is the rotation of the sulfur complex, resulting in the breakage of a SOH–Cu bond and, at the same time, the formation of a SO–Cu bond. This step has a barrier of 0.39 eV and is 0.41 eV lower in energy. The stable  $\text{CuHSO}_3$  complex (structure IV) is 0.55 eV more stable compared to physisorbed  $\text{SO}_2$  (structure II).

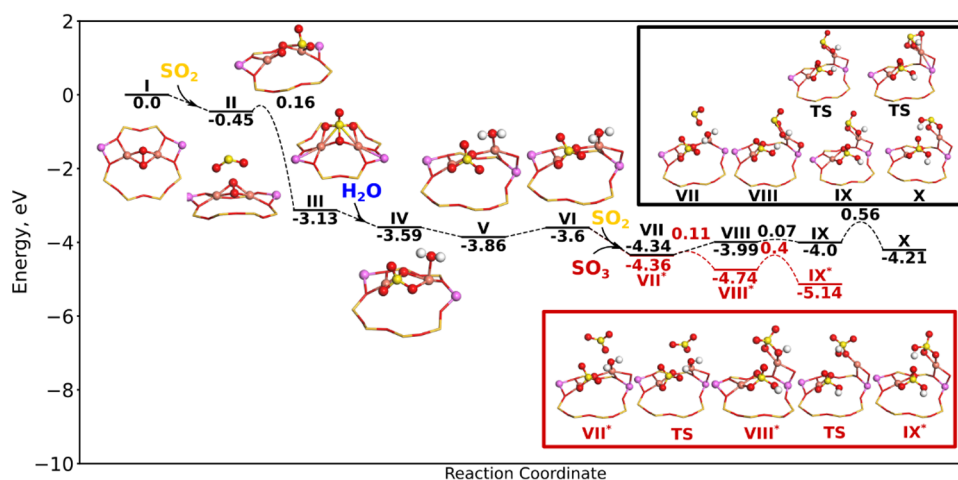


**Figure 2.** Energy landscape for the reaction of  $\text{SO}_3$  and  $\text{SO}_2$  with  $\text{Z}_2\text{CuO}_2\text{Cu}$  and the subsequent formation of  $\text{ZCuHSO}_x$  complexes. Atomic color codes are as in Figure 1.

The reaction of  $\text{SO}_3$  with  $\text{ZCuOH}$  is shown in Figure 1d. Physisorption of  $\text{SO}_3$  is exothermic by 0.56 eV (I  $\rightarrow$  II).  $\text{SO}_3$  can react with  $\text{ZCuOH}$  forming a  $\text{CuHSO}_4$  complex that is 0.77 eV more stable and associated with a barrier of 0.16 eV (II  $\rightarrow$  III). The following steps are connected to the reorientation of the  $\text{CuHSO}_4$  complex away from the eight-membered ring. The first step has a barrier of 0.13 eV and is endothermic by 0.08 eV (III  $\rightarrow$  IV). The second step has a barrier of 0.12 eV and is exothermic by 0.33 eV (IV  $\rightarrow$  V). The last step is the rotation of the  $\text{CuHSO}_4$  complex, resulting in the breakage of a  $\text{SOH-Cu}$  bond and the formation of a  $\text{SO-Cu}$  bond (V  $\rightarrow$  VI). The final  $\text{CuHSO}_4$  complex (structure VI) is 1.3 eV more stable than physisorbed  $\text{SO}_3$  (structure II).

For  $\text{ZCuOH}$ , the same trend as for  $\text{Z}_2\text{Cu}$  is observed, where  $\text{SO}_3$  forms more stable sulfur complexes (−1.3 versus −0.55 eV), which is associated with lower activation barriers compared to the  $\text{SO}_2$ -derived sulfur complexes (0.22 versus 0.39 eV).

As the  $\text{SO}_x$  exposure is performed in the presence of  $\text{O}_2$  at 400 °C, a pair of Cu ions may adsorb  $\text{O}_2$  forming framework-bound peroxy species,  $\text{Z}_2\text{CuO}_2\text{Cu}$ .<sup>74</sup> The reaction landscape for the reaction of  $\text{SO}_2$  and  $\text{SO}_3$  with  $\text{Z}_2\text{CuO}_2\text{Cu}$  is shown in Figure 2. The starting structure I could originate from a pair of  $\text{Cu}^+$  ions that adsorb  $\text{O}_2$ .<sup>74</sup>  $\text{SO}_2$  cannot adsorb directly onto the complex (structure II). Instead,  $\text{SO}_2$  can react (low barrier of 0.16 eV) with the adsorbed  $\text{O}_2$  molecule forming a stable  $\text{Z}_2\text{Cu}(\text{SO}_4)\text{Cu}$  complex (II  $\rightarrow$  III), which is 2.68 eV more stable. During the reaction, sulfur is oxidized from +4 to +6. The strongly exothermic nature of sulfur oxidizing for Cu-CHA has been observed previously for  $\text{SO}_2$  oxidation over the mobile peroxy complex  $[\text{Cu}_2\text{O}_2(\text{NH}_3)_4]^{2+}$ .<sup>57</sup> The Cu ions remain in a +2 oxidation state, supplying the two electrons needed to form the sulfate species ( $\text{SO}_4^{2-}$ ). This complex cannot react directly with  $\text{SO}_2$  or  $\text{SO}_3$ ; however, in the presence of  $\text{H}_2\text{O}$ , it is possible to form  $\text{CuHSO}_3$  and  $\text{CuHSO}_4$  complexes.  $\text{H}_2\text{O}$  can adsorb onto Cu with a binding energy of 0.46 eV (III  $\rightarrow$  IV). The next step is the breakage of a  $\text{SO-Cu}$  bond (IV  $\rightarrow$  V). Furthermore, a bond between Cu and an oxygen in the framework ( $\text{O}_{\text{fw}}$ ) is broken and a new  $\text{Cu-O}_{\text{fw}}$  bond is formed. The configuration of structure V is favored for the formation of sulfur complexes. The next step (V  $\rightarrow$  VI) is endothermic by 0.26 eV and is the result of the coordination of hydrogen from  $\text{H}_2\text{O}$ , which changes from one oxygen to

another that is bonded to sulfur. The next steps follow two different paths, which involves the reaction with either  $\text{SO}_2$  or  $\text{SO}_3$  indicated in black or red with a star (\*), respectively.  $\text{SO}_2$  (black) can react with  $\text{H}_2\text{O}$ , splitting the O–H bond of  $\text{H}_2\text{O}$  and forming a  $\text{CuHSO}_3$  and  $\text{CuHSO}_4$  complex (VII  $\rightarrow$  VIII), which is endothermic with 0.35 eV. The next step (VIII  $\rightarrow$  IX) is the change of the coordination of an OH group bound to sulfur, which is turned away. The last step is the rotation of  $\text{CuHSO}_3$  that leads to the breakage of a  $\text{SOH-Cu}$  bond and formation of a  $\text{SO-Cu}$  bond (IX  $\rightarrow$  X). This step has a barrier of 0.56 eV and is exothermic by 0.21 eV. From structure VI, it is also possible to follow the structure denoted with an \*, which is the reaction with  $\text{SO}_3$ . Here,  $\text{SO}_3$  can react with  $\text{H}_2\text{O}$  forming two  $\text{CuHSO}_4$  complexes (VII\*  $\rightarrow$  VIII\*). The formation of  $\text{CuHSO}_4$  is associated with a small barrier of 0.11 eV and is exothermic by 0.38 eV. As in the previous case, the next step involves the rotation of  $\text{HSO}_4$ , so the  $-\text{SOH}$  group is no longer bonded to Cu (VIII\*  $\rightarrow$  IX\*). The rotation has a barrier of 0.4 eV and is exothermic by 0.4 eV.

From the reaction landscapes, we conclude that more stable sulfur complexes are formed when reacting  $\text{Z}_2\text{CuO}_2\text{Cu}$  with  $\text{SO}_3$  compared to  $\text{SO}_2$ . This is similar to the reactions on  $\text{Z}_2\text{Cu}$  and  $\text{ZCuOH}$ . In addition, the activation barriers associated with the reaction with  $\text{SO}_3$  are lower than for  $\text{SO}_2$ . Compared to  $\text{Z}_2\text{Cu}$  and  $\text{ZCuOH}$ , the first reaction with  $\text{SO}_2$  (II  $\rightarrow$  III) forms more stable complexes suggesting that  $\text{Z}_2\text{CuO}_2\text{Cu}$  causes more severe deactivation. To form  $\text{Z}_2\text{CuO}_2\text{Cu}$ , the catalyst must be exposed to  $\text{O}_2$ . When  $\text{SO}_2$  is cofed with  $\text{O}_2$ , severe deactivation has been experimentally observed,<sup>49</sup> which is consistent with our calculations. Furthermore, it is possible to oxidize  $\text{SO}_2$  to  $\text{SO}_4^{2-}$  over the  $\text{Z}_2\text{CuO}_2\text{Cu}$  and the presence of sulfur in +6 oxidation states has been observed using X-ray absorption spectroscopy.<sup>78</sup> The sulfur-derived complexes formed when reacting  $\text{SO}_x$  with  $\text{Z}_2\text{CuO}_2\text{Cu}$  are the same as those for the cases with  $\text{Z}_2\text{Cu}$  and  $\text{ZCuOH}$ . This indicates that even though more sulfur complexes may form on  $\text{Z}_2\text{CuO}_2\text{Cu}$ , it is difficult to unravel the origin of the species. However, the proximity of two  $\text{CuHSO}_4$  ions could potentially stabilize the complexes. The observation that  $\text{SO}_3$  forms more stable sulfur complexes that are associated with lower barriers compared to  $\text{SO}_2$  for all Cu sites is consistent with the observation of more  $\text{SO}_x$  release in TPD experiments.<sup>9</sup> In addition, it is observed

that  $\text{SO}_3$  in general causes more deactivation of the low-temperature  $\text{NH}_3\text{-SCR}$ .<sup>9</sup>

### 3.2. Elemental Analysis, $\text{N}_2$ Physisorption, and XRD Analysis of Powder Cu/SSZ-13

Elemental analysis and  $\text{N}_2$  physisorption were conducted for the prepared copper-exchanged SSZ-13 powders, and the results for the degreened samples are shown in Table S1. SAR (Si/Al molar ratio) was around 14, and the Cu content was 0.83 wt %. The BET surface area decreased (from 711 to 651  $\text{m}^2\cdot\text{g}^{-1}$ ) after impregnation of Cu ions. With respect to sulfated samples, 33 and 159  $\mu\text{mol}\cdot\text{g}_{\text{washcoat}}^{-1}$  of sulfur content were obtained for  $\text{SO}_2$ - and  $\text{SO}_3$ -exposed samples, respectively. In Figure S3, a comparison of X-ray diffractograms for the degreened H and Cu forms of SSZ-13 shows that the CHA framework structure was well maintained without noticeable diffraction peaks of  $\text{Cu}_x\text{O}_y$  crystalline particles ( $36.30$  and  $38.72^\circ 2\theta$ )<sup>5</sup> or  $\text{Cu}(\text{OH})_2$  precipitates ( $12.83$  and  $25.84^\circ 2\theta$ )<sup>37</sup> in the sample powders. Note that the fresh sample was degreened in standard SCR conditions at  $750^\circ\text{C}$  for 5 h and a low Cu loading amount was set (ca. 1 wt % Cu) to avoid possible formation of copper-containing particles. This suggests that no or minor amounts of  $\text{Cu}_x\text{O}_y$  particles were formed and if any was formed; they were below the detection limit of the XRD. It is, thus, assumed that most copper is present as isolated Cu ions interacting with 1 or 2  $\text{Al}_\text{I}$  over the CHA structure of the degreened powder.

The effect of  $\text{SO}_2$  and  $\text{SO}_3$  exposure to Cu-CHA was examined using SEM and XRD with the following sulfation sequence: (i)  $\text{SO}_2/\text{SO}_3+\text{O}_2+\text{H}_2\text{O}$ ; (ii)  $\text{NH}_3 + \text{O}_2+\text{H}_2\text{O}$  and (iii)  $\text{SO}_2/\text{SO}_3+\text{O}_2+\text{H}_2\text{O}$ . We confirmed that no clear changes in crystal morphology from  $\text{SO}_2$ - and  $\text{SO}_3$ -exposed samples using SEM (see Figure S4) were observed compared to the degreened sample. XRD data are shown in Figure 3, and for the degreened sample, catalyst powder was used while for the  $\text{SO}_2$  and  $\text{SO}_3$ -exposed samples, washcoat was scraped off from the monoliths. In addition, XRD of the cordierite is shown and it is clear that the cordierite present in the samples that were

scraped off the monoliths can be neglected. The XRD results show shifted diffraction peaks (Figure 3). The inset (dashed purple) in Figure 3 represents the region of crystallographic planes containing  $[1\ 0\ 0]$  (ca.  $9.5^\circ$ ),  $[-1\ 1\ 0]$  (ca.  $13^\circ$ ), and  $[1\ 1\ 0]$  ( $14^\circ$ ).<sup>46</sup> Both  $\text{SO}_2$ - and  $\text{SO}_3$ -exposed samples caused peak shifting toward either lower or higher angles compared to the degreened sample, respectively. This suggests that  $\text{SO}_2$  and  $\text{SO}_3$  exposure at  $400^\circ\text{C}$  results in changes of the CHA unit cell size but no damaged framework structure according to Bragg's law.<sup>79</sup> Decreased peak intensity for  $\text{SO}_2$ - and  $\text{SO}_3$ -exposed samples indicates that sulfur species were successfully introduced into the CHA unit cell. However, questions remain as to why  $\text{SO}_2$  and  $\text{SO}_3$  caused different trends in the shift of the peak toward lower and higher angles, respectively. This different peak shifting trend implies that different lattice distances resulted from  $\text{SO}_2$  and  $\text{SO}_3$  exposure with  $\text{NH}_3$  oxidation as the middle step.

UV–visible diffuse reflectance spectroscopy (UV–vis-DRS) was performed to investigate possible formation of different sulfur species. Reference UV spectra were measured for copper compounds (i.e.,  $\text{CuSO}_4$ ,  $\text{Cu}(\text{OH})_2$ ,  $\text{CuO}$ ) and various ammonium (bi)sulfite/sulfate in hydrated and ambient conditions, as shown in Figure S5. Figure 4 presents the resulting UV spectra as a function of wavelength for degreened and  $\text{SO}_2$ - and  $\text{SO}_3$ -exposed samples. Figure 4a shows for all samples two typical UV absorption features corresponding to the d–d transition of hydrated  $\text{Cu}^{2+}$  ions (ca. at 800 nm) and the ligand to metal charge transfer (LMCT) transition caused by the isolated  $\text{Cu}^{2+}$  ions (lattice  $\text{O} \rightarrow \text{Cu}^{2+}$ , at ca. 220 nm) of Cu/SSZ-13, as reported in literature.<sup>49,80,81</sup> Moreover, UV absorption was observed for both  $\text{SO}_2$ - and  $\text{SO}_3$ -exposed samples over the entire measured wavelength, which was not the case for the degreened sample. This suggests the presence of ammonium (bi)sulfite/sulfate species since these species display considerable UV absorbance over the entire wavelength, as shown in Figure S5b. Both  $\text{SO}_2$ - and  $\text{SO}_3$ -exposed samples show in addition a broader UV absorption band at 250–300 nm compared to the degreened sample. The first derivative of Figure 4a was applied to qualitatively examine the effect of  $\text{SO}_2$  and  $\text{SO}_3$  with  $\text{NH}_3$  oxidation as a middle step, as shown in Figure 4b. The result shows different features of the  $\text{SO}_2$ - and  $\text{SO}_3$ -exposed samples compared to the degreened sample, especially at 220–400 nm. Dissimilar UV absorption features between the  $\text{SO}_2$ - and  $\text{SO}_3$ -exposed samples as in Figure 4c indicates the possible formation of different types of sulfur species interacting with  $\text{NH}_3$ .

In comparison with reference bulk materials in Figure S5,  $\text{CuSO}_4$  (Figure S5a) and various ammonium (bi)sulfites/sulfates (Figure S5b) were considered as potentially formed sulfur species arising during  $\text{SO}_2$  and  $\text{SO}_3$  exposure. In the region of 220–400 nm, the broad UV absorbance for  $\text{CuSO}_4$  and ammonium (bi)sulfite/sulfate indicates that copper sulfate can be potential sulfur species interacting with  $\text{Cu}^{2+}$  ions, and the observed additional absorbance (shoulder at 250–300 nm in Figure 4a) is likely to originate from ammonium sulfate ( $(\text{NH}_4)_2\text{SO}_4$ ) or ammonium sulfite ( $(\text{NH}_4)_2\text{SO}_3$ ). To exclude the background resulting from Cu-CHA with respect to the  $\text{SO}_2$ - and  $\text{SO}_3$ -exposed samples, the UV spectrum of the degreened sample was subtracted from the  $\text{SO}_2$ - and  $\text{SO}_3$ -exposed samples. In Figure 4c, the resulting first derivative of UV absorbance shows the comparison of the derived sulfur species during the  $\text{SO}_2$  and  $\text{SO}_3$  exposure with  $\text{NH}_3$  saturation. By comparing the reference samples (i.e., bulk ammonium

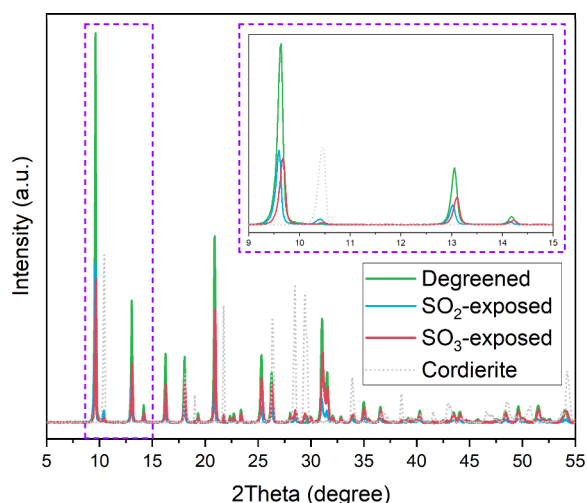


**Figure 3.** X-ray diffractogram for degreened and  $\text{SO}_2$ - and  $\text{SO}_3$ -exposed samples. The  $\text{SO}_2$ - and  $\text{SO}_3$ -exposed samples were scraped off the washcoat from monoliths. In addition, XRD from pure cordierite is shown. The inset illustrates X-ray diffraction peak shifting in the position of crystallographic planes with indices of  $[1\ 0\ 0]$  (ca.  $9.5^\circ$ ),  $[-1\ 1\ 0]$  (ca.  $13^\circ$ ), and  $[1\ 1\ 0]$  (ca.  $14^\circ$ ).



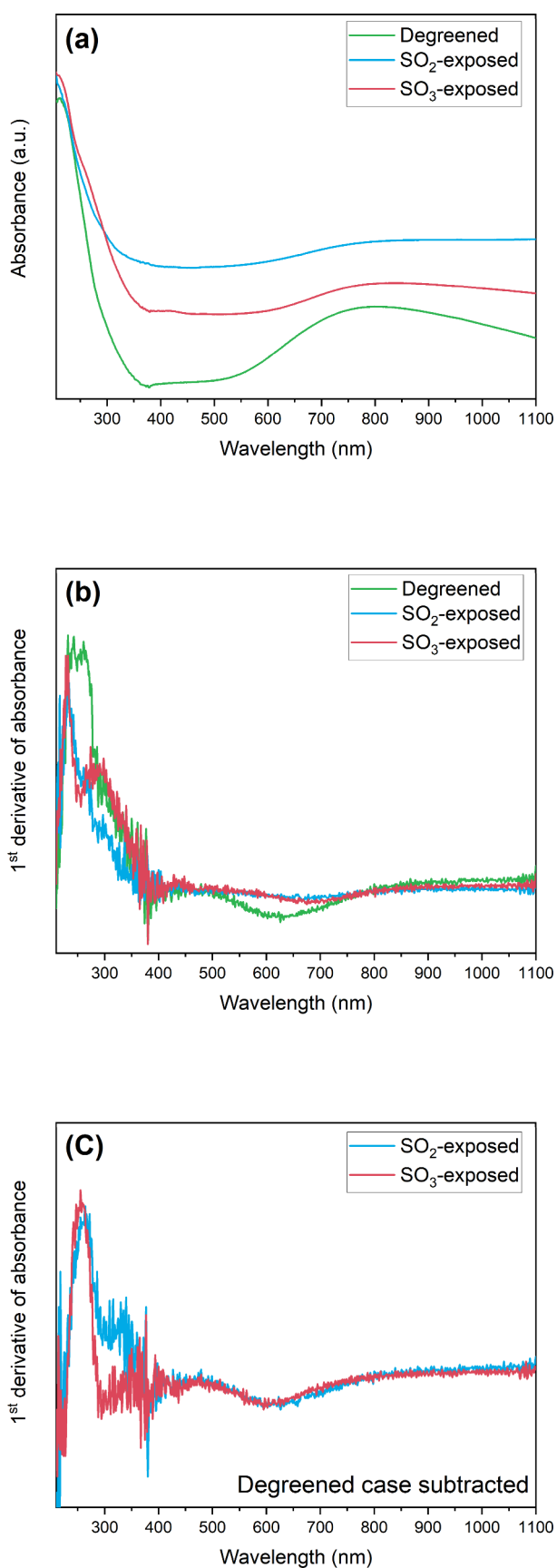


**Figure 4.** UV–visible diffuse reflectance spectra for degreened and  $\text{SO}_2$ - and  $\text{SO}_3$ -exposed powder samples in terms of (a) absorbance, (b) first derivative of absorbance, and (c) first derivative of absorbance with the degreened sample subtracted.

(bi)sulfite/sulfate) in Figure S5d, the result implies that the  $\text{SO}_2$  and  $\text{SO}_3$  exposures, with  $\text{NH}_3$  oxidation as the middle step, are associated with the formation of ammonium sulfite ( $(\text{NH}_4)_2\text{SO}_3$ ), ammonium sulfate ( $(\text{NH}_4)_2\text{SO}_4$ ), or (bi)sulfate ( $(\text{NH}_4)\text{HSO}_4$ ).

### 3.3. $\text{H}_2$ TPR in Degreened and $\text{SO}_2$ - and $\text{SO}_3$ -Exposed Cu/SSZ-13

XRD and UV–vis-DRS results suggest that different sulfated species are interacting with  $\text{NH}_3$  and copper ions inside the CHA unit cell, resulting from  $\text{SO}_2$  and  $\text{SO}_3$  exposure of Cu-CHA (with ammonia oxidation as a middle step). This implies that the formed sulfated species can influence the reduction properties of isolated  $\text{Cu}^{2+}$  ions. Bergman et al.<sup>60</sup> showed that  $\text{SO}_2$  exposure influences the reduction property of  $\text{Cu}^{2+}$  in Cu-CHA using in situ XAS. Thus,  $\text{H}_2$  temperature-programmed reduction ( $\text{H}_2$ -TPR) was carried out to investigate the reduction property of the  $\text{SO}_2$ - and  $\text{SO}_3$ -exposed samples.

Figure 5a shows  $\text{H}_2$  consumption as a function of temperature for degreened and  $\text{SO}_2$ - and  $\text{SO}_3$ -exposed samples. The degreened sample shows  $\text{H}_2$  consumption in the temperature range of 200–650 °C, resulting from  $\text{Cu}^{2+}$  species reduction by  $\text{H}_2$ . In general,  $\text{ZCuOH}$  and  $\text{Z}_2\text{Cu}$  are regarded as primarily isolated  $\text{Cu}^{2+}$  species over Cu-CHA and the observed  $\text{H}_2$  consumption peaks are commonly assigned to  $\text{ZCuOH}$  and  $\text{Z}_2\text{Cu}$  at low and high temperatures, respectively, due to different binding strengths of  $\text{Cu}^{2+}$  species interacting with the CHA framework.<sup>5,48,73,82,83</sup> In addition, in our recent study, combining ab initio calculations with experimental results, we also found the importance  $\text{Z}_2\text{CuOCu}$ ,  $\text{Z}_2\text{CuHOOCu}$ , and  $\text{Z}_2\text{CuOOCu}$  to describe the reduction process.<sup>84</sup>

For the degreened sample in Figure 5a, the main reduction peak at 430 °C was impeded due to sulfur species, implying an interaction between sulfur and copper species. In contrast to the degreened sample, the sulfated samples show larger  $\text{H}_2$  consumption.  $\text{SO}_2$  and  $\text{NH}_3$  signals were detected as shown in Figure 5b,c, suggesting that  $\text{SO}_2$  and  $\text{NH}_3$  originated from decomposition of the remaining ammonium (bi)sulfite/sulfate species. The  $\text{SO}_2$ -exposed sample shows two distinct reduction features during  $\text{H}_2$  TPR at ca. 293 and 652 °C (Figure 5a). For the  $\text{SO}_3$ -exposed sample, relatively intense reduction peaks were observed at 657 °C with a shoulder (604 °C) and at 293 °C. The  $\text{SO}_3$ -exposed sample showed three distinct  $\text{H}_2$  consumption peaks at 293, 604, and 657 °C, but only two reduction peaks corresponding to ca. 293 and 652 °C were observed for the  $\text{SO}_2$ -exposed sample. Thus, it is likely that the peak at 293 °C resulted from hydrogen reacting with ammonium sulfite/sulfate species and the peaks at 604 and 657 °C originated from sulfur species interacting with  $\text{Cu}^{2+}$  ions since  $\text{SO}_2$  started to be observed above 400 °C with a peak at 577 °C in Figure 5b. In addition, an  $\text{H}_2\text{S}$  (mass 34) was measured and a weak signal was detected above 650 °C for the  $\text{SO}_3$ -exposed sample in Figure S6. Based on this, we suggest that the main hydrogen consumption peak at 657 °C might be associated with  $\text{H}_2\text{S}$  formation since it requires a two-electron transfer to form  $\text{H}_2\text{S}$  as well as cleavage of S–O/S=O bonds to become the sulfide ( $\text{S}^{2-}$ ) of  $\text{H}_2\text{S}$ . It should be noted that the detection of  $\text{H}_2\text{S}$  in the MS is rather difficult, and we suggest that this is the reason for the significantly smaller and noisier  $\text{H}_2\text{S}$  peak compared to the hydrogen consumption peak. In contrast, no  $\text{H}_2\text{S}$  signal was observed for the  $\text{SO}_2$ -exposed sample. This is probably because of the lower amount of  $\text{H}_2\text{S}$

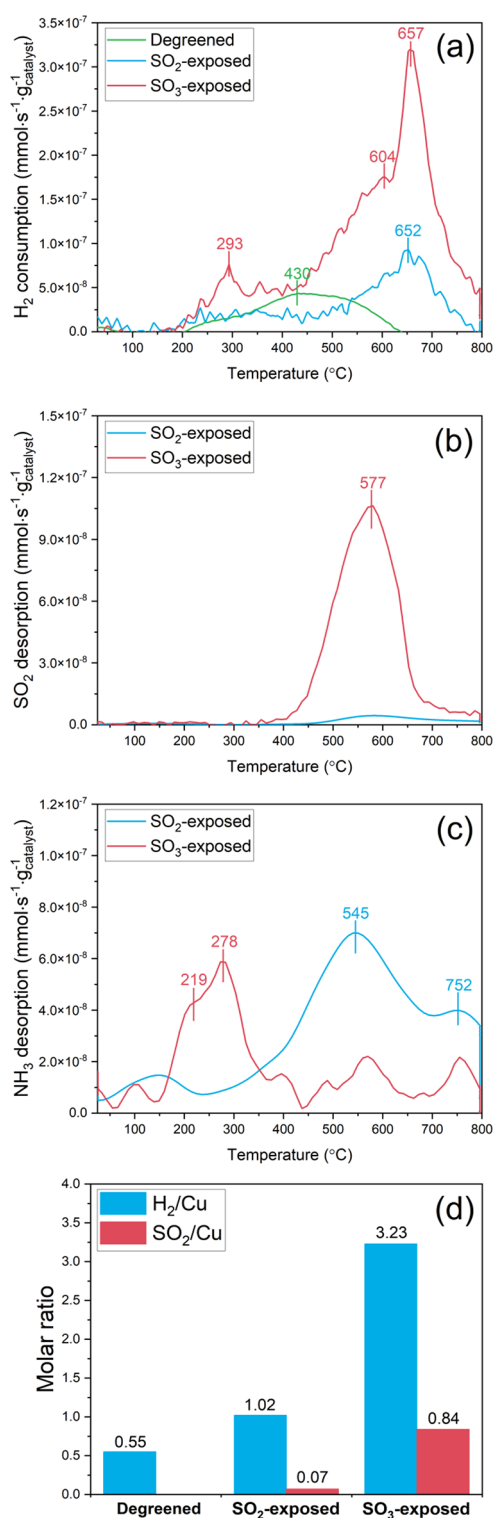


**Figure 5.**  $\text{H}_2$  temperature-programmed reduction for degreened and  $\text{SO}_2$ - and  $\text{SO}_3$ -exposed samples showing  $\text{H}_2$  consumption (a), desorption of  $\text{SO}_2$  (b), and  $\text{NH}_3$  release (c), and molar ratios of consumed  $\text{H}_2$  and desorbed  $\text{SO}_2$  per Cu content of samples (hydrated condition, gas feed: 0.2%  $\text{H}_2/\text{Ar}$ , heating rate:  $10\text{ }^\circ\text{C}\cdot\text{min}^{-1}$ , total flow rate:  $20\text{ N mL}\cdot\text{min}^{-1}$ ).

formation as a result of the relatively lower sulfur content in the  $\text{SO}_2$ -exposed sample compared to the  $\text{SO}_3$ -exposed sample according to the ICP results in Section S3, SI. Both  $\text{SO}_2$ - and  $\text{SO}_3$ -exposed samples showed an  $\text{SO}_2$  desorption, with a single

peak in the same temperature region (peak at  $577\text{ }^\circ\text{C}$ ) (see Figure 5b). However, the sulfur release from the  $\text{SO}_3$ -exposed sample was significantly larger. Note that  $\text{H}_2\text{SO}_4$  and  $\text{SO}_3$  signals were not detected during  $\text{H}_2$ -TPR but these compounds would be challenging to detect in the calorimeter setup if they are in low concentrations. In addition, ammonia desorption was clear from both  $\text{SO}_2$ - and  $\text{SO}_3$ -exposed samples, with two desorption peaks Figure 5c.

The consumed  $\text{H}_2$  per Cu and  $\text{SO}_2$  release per Cu from the  $\text{H}_2$  TPR are shown in Figure 5d. For the degreened sample without sulfur added, the  $\text{H}_2/\text{Cu}$  ratio is 0.55, indicating that a one-step reduction of copper occurred. This is common at these temperatures, since a full reduction to metallic copper usually requires higher temperatures. Larger  $\text{H}_2$  consumption is found for the  $\text{SO}_2$ -exposed sample, which is significantly increased for the  $\text{SO}_3$ -exposed sample, simultaneously with the  $\text{SO}_2$  desorption increasing. Larger  $\text{H}_2/\text{Cu}$  and  $\text{SO}_2/\text{Cu}$  ratios are expected if the  $\text{SO}_x$ -exposed sample involves a larger sulfur content. Figure 5d suggests that  $\text{SO}_3$  exposure results in a much larger sulfur uptake compared to  $\text{SO}_2$  exposure. This is in line with the ICP analysis results regarding the sulfur content (Section S3, SI). Considering the observed  $\text{NH}_3$  release and  $\text{SO}_2$  desorption features in Figure 5b,c, it can be concluded that  $\text{NH}_3$ -sulfur interacting species remained following the sulfation and ammonia exposure step at  $400\text{ }^\circ\text{C}$ . Different sulfur speciation is expected to result from the  $\text{SO}_2$  and  $\text{SO}_3$  exposure, with  $\text{NH}_3$  as a middle step, forming ammonium sulfite ( $(\text{NH}_4)_2\text{SO}_3$ ) and ammonium sulfate ( $(\text{NH}_4)_2\text{SO}_4$ ) or (bi)sulfate ( $(\text{NH}_4)\text{HSO}_4$ ) species according to the UV–vis DRS results.

### 3.4. AN-TPD with Degreened and $\text{SO}_2$ - and $\text{SO}_3$ -Exposed Cu/SSZ-13

AN can easily be formed from  $\text{NO}_2$  and  $\text{NH}_3$ , and during its decomposition, it is well known that  $\text{N}_2\text{O}$  is formed. Normally, a larger amount of  $\text{N}_2\text{O}$  is reported as the  $\text{NO}_2$  concentration is increased during SCR reaction.<sup>35</sup> We have reported increased  $\text{N}_2\text{O}$  formation for Cu-CHA compared to H-CHA, indicating that AN interacts with copper species.<sup>5</sup> It is, therefore, expected that  $\text{SO}_2$  and  $\text{SO}_3$  influence the AN and  $\text{N}_2\text{O}$  formation.

Temperature-programmed desorption with AN (AN-TPD) was carried out for degreened and  $\text{SO}_2$ - and  $\text{SO}_3$ -exposed samples to investigate the effects of  $\text{SO}_2$  and  $\text{SO}_3$  on AN and  $\text{N}_2\text{O}$  formation. The mass 28 ( $\text{N}_2$ ) signal was detected, while 200 ppm of  $\text{NH}_3/\text{NO}_2$  was fed for 90 min in the empty-tube test (see Figure S7). This suggests that the  $\text{NO}_2$  SCR occurred during the ionization process in the mass spectrometer. In addition, no  $\text{N}_2\text{O}$  signal was seen during heating when measuring with the FTIR as shown in Figure S7, suggesting that no AN was formed in the reactor system. The results for AN-TPD over Cu/SSZ-13 are presented in Figure 6. The  $\text{NH}_3$  concentrations during heating are presented in Figure 6a, where the  $\text{NH}_3$  release was increased for  $\text{SO}_2$ - and  $\text{SO}_3$ -exposed samples compared to the degreened samples. An increased  $\text{NH}_3$  release is expected due to residual sulfur species, since ammonium (bi)sulfite/sulfate species could form during the  $\text{NH}_3+\text{NO}_2$  feed period of the AN-TPD test. These results are in line with the studies in the literature,<sup>43,58,85,86</sup> where ammonia was suggested to interact with sulfate species resulting in larger ammonia storage. Notably, the  $\text{SO}_3$ -exposed sample shows the largest  $\text{NH}_3$  release; furthermore, its  $\text{NH}_3$

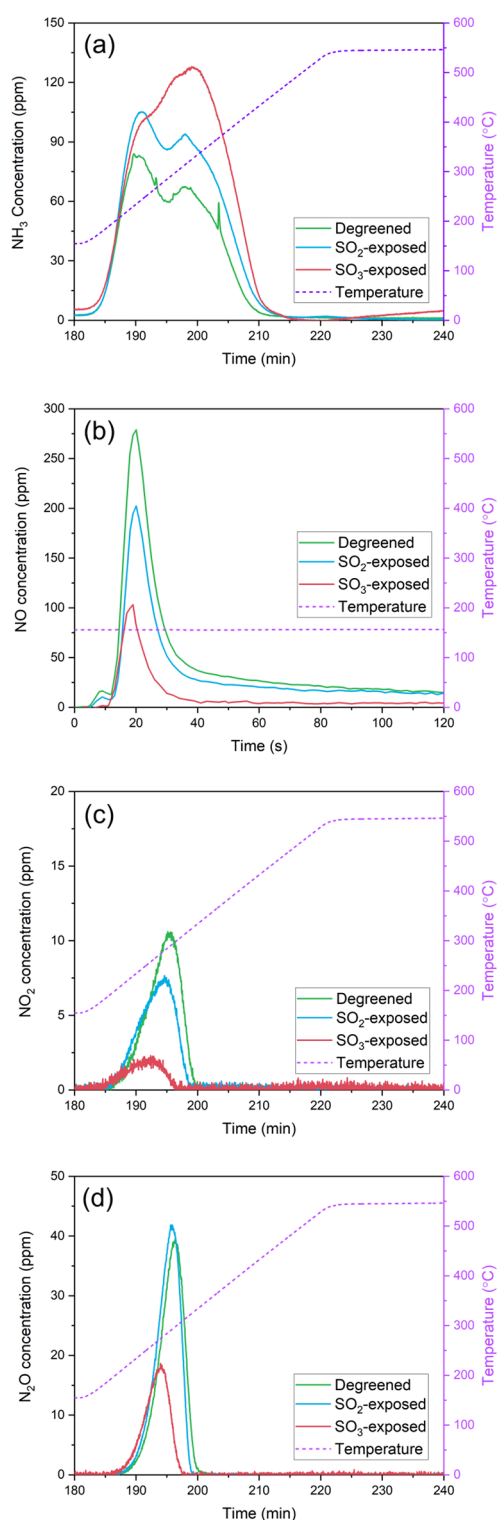


**Figure 6.**  $\text{NH}_3$  (a), NO (b),  $\text{NO}_2$  (c), and  $\text{N}_2\text{O}$  (d) concentrations during ammonium nitrate temperature-programmed desorption for degreened and  $\text{SO}_2$ - and  $\text{SO}_3$ -exposed samples (gas feed: 200 ppm of  $\text{NH}_3/\text{NO}_2 + 5\% \text{H}_2\text{O} + \text{Ar}$  at  $150^\circ\text{C}$  during adsorption, heating rate:  $10^\circ\text{C}\cdot\text{min}^{-1}$ , total flow rate:  $1200 \text{ N mL}\cdot\text{min}^{-1}$ ). Note that the NO concentration is during the adsorption phase.

release peak is also shifted from lower to higher temperatures compared to that for the  $\text{SO}_2$ -exposed and degreened samples.

Figure 6b shows the NO formation curves during  $\text{NH}_3 + \text{NO}_2$  adsorption for degreened and  $\text{SO}_2$ - and  $\text{SO}_3$ -exposed samples.

It has been reported that NO formation originates from  $\text{NO}_2$  disproportionation and subsequent surface nitrite oxidation by  $\text{NO}_2$ , leading to surface nitrate formation with gas-phase NO release.<sup>87–89</sup> The ratios for NO formed divided by removed  $\text{NO}_2$  during the adsorption phase were 0.03, 0.03, and 0.01 for the degreened,  $\text{SO}_2$ -exposed, and  $\text{SO}_3$ -exposed samples, respectively. A ratio of 0.33 is expected due to the disproportionation reaction where nitrates are formed.<sup>89</sup> Thus, these values are significantly lower and the reason for this is likely that we also have slow  $\text{NO}_2$  SCR occurring at this temperature, since we use a quite high temperature ( $150^\circ\text{C}$ ) and a large amount of the  $\text{NO}_2$  that is consumed is due to the SCR reaction. NO formation was decreased for both  $\text{SO}_2$ -exposed and, in particular,  $\text{SO}_3$ -exposed samples compared to the degreened sample. This suggests that surface nitrate storage was decreased due to sulfur species interacting with copper species since sulfur species do not show noticeable interaction with Brønsted sites.<sup>45</sup> In this respect, it is postulated that most surface nitrate was formed on copper species under these conditions (presence of water, for example), since significantly reduced NO formation was observed for the  $\text{SO}_3$ -exposed sample containing the largest sulfur content. Indeed, lower  $\text{NO}_2$  formation during the heating is found (Figure 6c), which is in line with the decreased surface nitrate storage, as  $\text{NO}_2$  formation is expected from the decomposition of the formed surface nitrate species during the  $\text{NH}_3 + \text{NO}_2$  adsorption.

Figure 6d shows  $\text{N}_2\text{O}$  formation during heating for the degreened and  $\text{SO}_2$ - and  $\text{SO}_3$ -exposed samples.  $\text{N}_2\text{O}$  formation due to thermal AN decomposition is commonly observed.<sup>90</sup> The  $\text{N}_2\text{O}$  curve from the  $\text{SO}_2$ -exposed sample shifted toward slightly lower temperatures compared to the degreened sample. Moreover, a similar amount of  $\text{N}_2\text{O}$  was released from the  $\text{SO}_2$ -exposed sample ( $31.9 \mu\text{mol}\cdot\text{g}^{-1}_{\text{washcoat}}$ ) as for the degreened sample ( $31.3 \mu\text{mol}\cdot\text{g}^{-1}_{\text{washcoat}}$ ). It is slightly more  $\text{N}_2\text{O}$  amount for the  $\text{SO}_2$ -exposed sample ( $\uparrow 1.9\%$ ), but the differences could be within the accuracy of the experiments. Despite similar  $\text{N}_2\text{O}$  formation, the  $\text{NO}_2$  release was clearly decreased for the  $\text{SO}_2$ -exposed sample (Figure 6c) as compared to that of the degreened sample, which we interpret as a result of nitrate decomposition. Thus, these results overall indicate that AN formation also decreased for the  $\text{SO}_2$ -exposed sample. However, it should be noted that some of the released  $\text{NO}_2$  could react in the slow  $\text{NO}_2$  SCR reaction. In contrast to the  $\text{SO}_2$ -exposed sample, the  $\text{SO}_3$ -exposed sample showed a remarkably decreased  $\text{N}_2\text{O}$  release ( $14.6 \mu\text{mol}\cdot\text{g}^{-1}_{\text{washcoat}}$ ) corresponding to a ca. 53% reduction in  $\text{N}_2\text{O}$  release compared to the degreened sample. The  $\text{N}_2\text{O}$  peak was also shifted toward lower temperatures compared to the  $\text{SO}_2$ -exposed and degreened samples. This suggests that  $\text{SO}_3$  exposure has a stronger influence on  $\text{N}_2\text{O}$  formation compared to  $\text{SO}_2$  exposure.

It should be mentioned that sulfur species such as  $\text{SO}_2$ ,  $\text{SO}_3$ ,  $\text{H}_2\text{SO}_4$ , and  $\text{H}_2\text{S}$  were measured by FTIR during AN-TPD. Among the sulfur species,  $\text{SO}_2$  and  $\text{H}_2\text{SO}_4$  were observed but the  $\text{SO}_3$  and  $\text{H}_2\text{S}$  were below the detection limit. However, a slightly negative  $\text{SO}_2$  signal (below 0 ppm) was observed from the  $\text{SO}_2$ - and  $\text{SO}_3$ -exposed samples that was symmetrical with the positive  $\text{H}_2\text{SO}_4$  curve, as shown in Figure S8. Thus, it is likely that there were overlapping bands in the FTIR that were slightly overcompensated by the software for  $\text{SO}_2$  and  $\text{H}_2\text{SO}_4$  according to Figure S9. To ease interpretation, the  $\text{H}_2\text{SO}_4$  and  $\text{SO}_2$  signals were merged as  $\text{SO}_2 + \text{H}_2\text{SO}_4$  (blue curve in Figure

S8), and sulfur species are denoted in this paragraph. The desorption of these sulfur species features was still maintained, showing three desorption peaks at 250, 368, and 537 °C for the SO<sub>2</sub>-exposed sample and a monotonically increasing SO<sub>2</sub>+H<sub>2</sub>SO<sub>4</sub> curve with a peak at 533 °C for the SO<sub>3</sub>-exposed sample. The marked different desorption features for these sulfur species suggests that SO<sub>3</sub> exposure causes more stable sulfur species compared to SO<sub>2</sub> exposure of Cu-CHA. For the SO<sub>2</sub>-exposed sample, the H<sub>2</sub>SO<sub>4</sub> peaks at 250 and 368 °C were located at same positions with two NH<sub>3</sub> release peaks at 180–215 min, as shown in Figure 6a. On the other hand, the SO<sub>3</sub>-exposed sample showed an even larger NH<sub>3</sub> release; however, there was no significant desorption of sulfur species during NH<sub>3</sub> release as compared to the SO<sub>2</sub>-exposed sample.

### 3.5. In Situ DRIFTS Measurement with Degreened and SO<sub>2</sub>- and SO<sub>3</sub>-Exposed Cu-CHA

AN-TPD results showed decreased NO formation during the NH<sub>3</sub>+NO<sub>2</sub> feed for the SO<sub>2</sub>- and SO<sub>3</sub>-exposed samples, implying that surface nitrite oxidation with NO<sub>2</sub> was severely limited. Especially, the SO<sub>3</sub>-exposed sample led to a considerably lower N<sub>2</sub>O formation. However, the SO<sub>2</sub>-exposed sample gave comparable N<sub>2</sub>O formation compared to the degreened sample, although less NO<sub>2</sub> formation was observed, consistent with that less AN was formed, as evident from the NO formation in the adsorption phase. To corroborate on these results, surface nitrite/nitrate species were investigated with DRIFTS in the presence of 400 ppm of NO<sub>2</sub> + 1% H<sub>2</sub>O + Ar at 150 °C. It should be mentioned that a relatively higher concentration of H<sub>2</sub>O is usually introduced to mimic the real exhaust environment. However, 1% H<sub>2</sub>O was set as the base feed here along with the background feed (Ar) since this was the maximum water feed in our DRIFTS setup. In addition, note that the powder sample was used for the degreened case, while crushed monoliths were used for the SO<sub>x</sub>-exposed monoliths. Thus, the sulfur exposed samples contain a large amount of cordierite and the spectra were therefore normalized with the amount of copper they contained.

Figure 7 shows the NO<sub>2</sub> adsorption phase for the degreened AND SO<sub>2</sub>- and SO<sub>3</sub>-exposed samples at 150 °C. The resulting spectral evolutions are illustrated in the region 2000–1000 cm<sup>-1</sup> to investigate the surface adsorption species. The surface nitrate region (1800–1500 cm<sup>-1</sup>) is magnified in the right panel from the original spectrum marked with the dashed line box. The addition of 400 ppm of the NO<sub>2</sub> + base feed mixture (Figure 7a) results in peaks related to the formation of chelating bidentate ZCu<sup>2+</sup>-(NO<sub>3</sub>) structures (1750–1500 cm<sup>-1</sup>).<sup>91</sup> The four bands at 1624, 1608, 1597, and 1575 cm<sup>-1</sup> are associated with  $\nu(\text{NO})$  vibrations of different types of chelating bidentate nitrates.<sup>91,92</sup> The peak at 1608 cm<sup>-1</sup> reached the highest intensity, when NO<sub>2</sub> was saturated (orange curve). Typical NO<sup>+</sup> formation (~2155 cm<sup>-1</sup>)<sup>93</sup> was not observed here under an excess of water, due to H<sub>2</sub>O interaction with Brønsted sites Si(OH)Al. The negative band (~1453 cm<sup>-1</sup>) is associated with H<sub>2</sub>O removal.<sup>94</sup> The band 1898 cm<sup>-1</sup> was assigned as NO interaction with Cu<sup>2+</sup> (i.e., Cu<sup>2+</sup>-NO).<sup>95</sup> Note that the negative peak (~1453 cm<sup>-1</sup>) may affect the neighboring nitrate feature.

For the SO<sub>2</sub>-exposed sample in Figure 7b, surface nitrate features were observed over the region 2000–1000 cm<sup>-1</sup>. The four bands associated with nitrate species (1629, 1611, 1597, and 1576 cm<sup>-1</sup>) were developed within 5 min and then consumed. Moreover, bands 1887 (positive band) and 1441

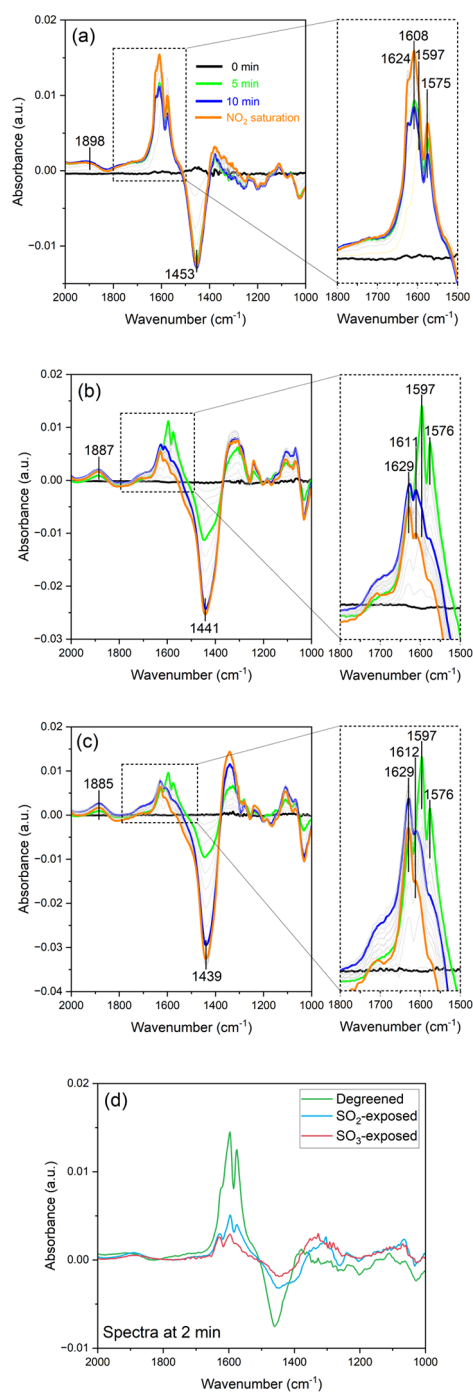


**Figure 7.** Spectrum evolution during NO<sub>2</sub> adsorption in DRIFTS for the (a) degreened, (b) SO<sub>2</sub>-exposed, and (c) SO<sub>3</sub>-exposed samples with (d) comparison of the NO<sub>2</sub> spectra of panels (a), (b), and (c) after 2 min of NO<sub>2</sub>+H<sub>2</sub>O exposure. Spectral evolution with gray represents intermediate spectra prior to NO<sub>2</sub> saturation (orange). Spectra in all panels were normalized by the number of moles of copper within the sample cup (gas feed: 400 ppm of NO<sub>2</sub> + 1% H<sub>2</sub>O + Ar at 150 °C, total flow rate: 100 N mL·min<sup>-1</sup>, sample bed temp.: 150 °C).

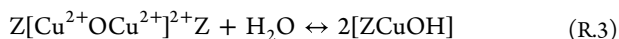
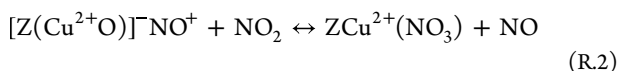
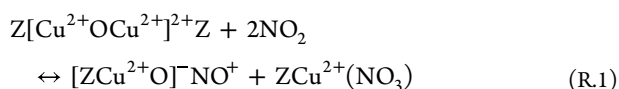
cm<sup>-1</sup> (negative band) were observed as well as the degreened sample. Surprisingly, at 10 min (blue curve), a decrease in the surface nitrate species peaks was observed, which were further decreased until NO<sub>2</sub> saturation (orange curve). During NO<sub>2</sub> adsorption, a decrease in the nitrates is not expected. The negative band at 1441 cm<sup>-1</sup>, due to water removal,<sup>94</sup> is quite

large. It is possible that there is an overlap between the 1441  $\text{cm}^{-1}$  negative band and the nitrate bands; thus, when the water removal increases, it decreases the bands in the nitrate region. This is not observed for the degreened sample, and the reason for that could be that the nitrate peaks are significantly larger; thus, the interference with the band at 1441  $\text{cm}^{-1}$  might be less. For the  $\text{SO}_3$ -exposed sample in Figure 7c, a similar trend was observed as the  $\text{SO}_2$ -exposed sample. For example, the surface nitrate region increased at 5 min (green curve), followed by decreased intensities until  $\text{NO}_2$  saturation (orange curve). Likewise, for the degreened sample, the positive band at 1885 and negative band at 1439  $\text{cm}^{-1}$  were observed. In Figure 7d, a comparison is done between the samples after only 2 min of  $\text{NO}_2 + \text{H}_2\text{O}$  exposure, where the water peaks for the  $\text{SO}_2$ - and  $\text{SO}_3$ -exposed samples are still quite small. From these results, it is clear that the nitrate bands are decreased for  $\text{SO}_2$ - and  $\text{SO}_3$ -exposed samples compared to the degreened sample.

To summarize, the DRIFT results show that there are fewer nitrates on the  $\text{SO}_2$ - and  $\text{SO}_3$ -exposed samples, as would be expected from the flow reactor experiments. However, it should be mentioned that there could be an overlap with the band for water removal, which could decrease the peak for nitrates.

#### 4. DISCUSSION

At low temperature, surface nitrate formation is observed in the presence of either  $\text{NO} + \text{O}_2$  or  $\text{NO}_2$  in Cu-CHA.<sup>89,91,92,96</sup> An in situ DRIFTS measurement shows that  $\text{NO}_2$  kinetically promotes surface nitrate formation in Cu-CHA compared to  $\text{NO} + \text{O}_2$  presence in dry conditions.<sup>89</sup> In wet conditions, the nitrate species formation is significantly hindered due to water interactions.<sup>89</sup>  $\text{NO}$  release is typically seen during isothermal  $\text{NO}_2$  adsorption in Cu-CHA, as shown in Figure 6b as well as in the literature,<sup>87,88,97,98</sup> resulting from surface nitrite oxidation by  $\text{NO}_2$ , and thereby,  $\text{NO}$  is formed through the following reactions (R.1 and R.2) below. According to Ruggeri et al.,<sup>89</sup> when  $\text{H}_2\text{O}$  is present, Cu dimers are likely dissociated into two  $\text{ZCuOH}$  via R.3.



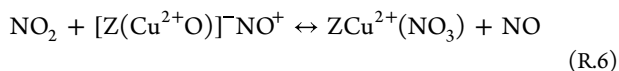
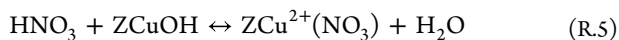
Ruggeri et al.<sup>89</sup> derived R.1–R.3 by  $\text{NO}$  or  $\text{NO}_2$  exposure to Cu-CHA at 120 or 150 °C in dry or wet conditions using in situ DRIFTS. Cu dimers in R.1 are critically important as a surface oxygen provider, initiating surface nitrite formation and leading to the additional nitrate in the form of copper nitrate and  $\text{NO}$  via R.2. A recent study performed by Negri et al.<sup>96</sup> reported that possible structures of nitrate species and their local environment show that only  $\text{ZCuOH}$  in the 8-MR within the CHA cage is the active copper species forming the framework-interacting chelating bidentate nitrate (i.e.,  $\text{Z}[\text{Cu}^{2+}(\text{NO}_3)]$ ).<sup>96</sup> Other nitrate candidates such as bridging bidentate or monodentate nitrate configurations were difficult to reconcile the experimental features under exposure of Cu-CHA to an  $\text{NO} + \text{O}_2$  mixture.<sup>91,96</sup>

The  $\text{SO}_2$  and  $\text{SO}_3$  exposure to Cu-CHA significantly influences the surface nitrate formation. In the AN TPD (Figure 6b), the  $\text{NO}$  release during isothermal  $\text{NH}_3 + \text{NO}_2$  adsorption is significantly decreased. Since  $\text{NO}$  production during  $\text{NO}_2$  exposure is associated with nitrate formation, according to reactions R.1 and R.2,<sup>89</sup> these results suggest that the surface nitrate formation is hindered due to resulting sulfur species after  $\text{SO}_2$  and  $\text{SO}_3$  treatment of Cu-CHA. The lowest  $\text{NO}$  release was observed for the  $\text{SO}_3$ -exposed sample (see Figure 6b), suggesting that this sample exhibited the lowest amount of nitrates, which is consistent with the fact that it contained the largest amount of sulfur, as seen in the ICP measurements (Section S3, SI). These results are also consistent with the in situ DRIFT experiments (see Figure 7d). Our first-principles calculations shown in Figure 1b,d describe that the  $\text{SO}_3$  interaction with both  $\text{Z}_2\text{Cu}$  and  $\text{ZCuOH}$  is possible. These findings are in agreement with ICP analysis showing an S/Cu molar ratio of 1.2, which indicates that all copper sites were occupied by sulfur species. In contrast,  $\text{SO}_2$  primarily interacts with  $\text{ZCuOH}$  but not  $\text{Z}_2\text{Cu}$  as suggested by first-principles calculations (Figure 1a,c). Since ICP results show low sulfur storage for the  $\text{SO}_2$ -exposed sample, it suggests that there is a low amount of  $\text{ZCuOH}$  in our sample. These results are consistent with our  $\text{H}_2$  TPR (Figure 5a) where the lower reduction peak, usually assigned to  $\text{ZCuOH}$ , is small for the degreened sample. A deconvolution of hydrogen TPR suggests only 15%  $\text{ZCuOH}$ . This value is slightly lower than the theoretical value according to Paolucci et al.,<sup>26</sup> which is 35%. The reason for this could be that in our synthesis of SSZ-13, we use Na cations and, according to Lee et al.,<sup>99</sup> SSZ-13 synthesis with the Na cation can increase 2Al sites over CHA. In our study, SSZ-13 was synthesized using Na and  $\text{TMAda}^+$ , and this could result in a larger amount of 2Al, which increases  $\text{Z}_2\text{Cu}$  and thereby decreases  $\text{ZCuOH}$ .

In terms of speciation of sulfur according to the first-principles calculation in Figures 1 and 2,  $\text{SO}_2$  interaction with  $\text{ZCuOH}$  results in (bi)sulfite ( $\text{ZCuHSO}_3$ ) and  $\text{SO}_2$  interactions with dicopper cause both (bi)sulfite and (bi)sulfate surface species. Meanwhile, the interaction of  $\text{SO}_3$  with  $\text{Z}_2\text{Cu}$  and  $\text{ZCuOH}$  leads to only (bi)sulfate ( $\text{ZCuHSO}_4$ ). The (bi)sulfate resulting from the  $\text{SO}_3$  exposure shows a lower energy compared to the other sulfur species (i.e.,  $\text{ZCuHSO}_3$ ) derived from the  $\text{SO}_2$  exposure. Importantly,  $\text{SO}_2$  and  $\text{SO}_3$  interaction with Cu dimers shows a further decrease in energy compared to the  $\text{SO}_2$  and  $\text{SO}_3$  adsorption with monomeric copper species (i.e.,  $\text{Z}_2\text{Cu}$  and  $\text{ZCuOH}$ ). The difference between the interaction of  $\text{SO}_2$  and  $\text{SO}_3$  with Cu dimers is that  $\text{SO}_2$  adsorption causes both  $\text{ZCuHSO}_3$  and  $\text{ZCuHSO}_4$ . The  $\text{SO}_3$  adsorption, however, results in only two  $\text{ZCuHSO}_4$ . In this respect, two  $\text{H}_2$  consumption peaks at 604 and 657 °C can be associated with (bi)sulfate interacting with copper monomers and dimers, respectively, in Figure 5a.

As mentioned above and described in reaction R.3, in the presence of water,  $\text{ZCuOH}$  is the active species for the surface nitrate formation in the form of copper nitrate ( $\text{ZCuNO}_3$ ) by following reactions below (R.4–R.6), as described in the refs 89,100. In the feed of only  $\text{NO}_2$ ,  $\text{NO}^+$  on the copper site results from  $\text{NO}_2$  disproportionation with forming nitric acid ( $\text{HNO}_3$ ) via R.4. In R.6, the resulting copper-nitrite oxidation by  $\text{NO}_2$  leads to copper nitrate and  $\text{NO}$ . For the  $\text{SO}_3$ -exposed sample, most copper sites are occupied by (bi)sulfate in the form of copper-(bi)sulfate ( $\text{ZCuHSO}_4$ ).  $\text{ZCuHSO}_4$ , therefore, deactivates the surface nitrate formation by blocking the

copper site from the access of the  $\text{NO}^+$  or  $\text{HNO}_3$ , resulting in the lowest NO release during the adsorption phase in AN-TPD. In the same manner, decreased NO release was seen for the  $\text{SO}_2$ -exposed sample compared with the degreened sample. However, more NO release was observed due to less sulfur content compared to the  $\text{SO}_3$ -exposed sample.



In AN-TPD, stored surface nitrate species are typically desorbed in the form of  $\text{NO}_2$  for the degreened sample, as can be seen in Figure 6c. For the  $\text{SO}_2$ - and  $\text{SO}_3$ -exposed samples, decreased  $\text{NO}_2$  release was seen because of decreased nitrate storage resulting from sulfur species, especially the  $\text{SO}_3$ -exposed sample. With respect to  $\text{N}_2\text{O}$ , the  $\text{SO}_3$ -exposed sample released the lowest amount of  $\text{N}_2\text{O}$  ( $14.6 \mu\text{mol}\cdot\text{g}^{-1}_{\text{washcoat}}$ ) compared to the  $\text{SO}_2$ -exposed sample ( $31.9 \mu\text{mol}\cdot\text{g}^{-1}_{\text{washcoat}}$ ).

Surprisingly, a comparable amount of  $\text{N}_2\text{O}$  was released for the  $\text{SO}_2$ -exposed sample as degreened sample ( $31.3 \mu\text{mol}\cdot\text{g}^{-1}_{\text{washcoat}}$ ), although decreased nitrate storage was clearly observed via NO formation in Figure 6b. This suggests that sulfur may increase  $\text{N}_2\text{O}$  selectivity during  $\text{NO}_2$  SCR. Sulfur enhances ammonia storage on the catalyst. We hypothesize that the increased availability of ammonia on the catalyst for the  $\text{SO}_2$  poisoned sample could result in that more  $\text{N}_2\text{O}$  is formed compared to  $\text{NO}_2$  release. According to first-principle calculations performed by Feng et al.,<sup>36</sup> the decomposition of the reaction intermediate ( $\text{H}_2\text{NNO}$ ) over the Cu site leads to  $\text{N}_2\text{O}$  and  $\text{H}_2\text{O}$ . Their suggested specific copper-configuration is  $\text{NH}_3$ -solvated Cu dimers. In Figure S8, the observed  $\text{SO}_2+\text{H}_2\text{SO}_4$  release and  $\text{N}_2\text{O}$  production (Figure 6d) show that for the  $\text{SO}_2$  poisoned sample, there is sulfur release already from 200 °C. The main  $\text{N}_2\text{O}$  desorption occurs at 300 °C, suggesting that some of the copper sites were regenerated for the  $\text{SO}_2$ -exposed sample; thus, resulting  $\text{H}_2\text{NNO}$  intermediates can possibly lead to  $\text{N}_2\text{O}$  through the regenerated copper sites. This combination with the increased availability of ammonia could be one possible explanation. However, for the  $\text{SO}_3$ -exposed sample, there was significantly more sulfur stored on the sample as seen in ICP experiments. In addition, the sulfate species were very stable, which is seen by the fact that the  $\text{SO}_2+\text{H}_2\text{SO}_4$  release occurred at significantly higher temperature and was not detected during  $\text{N}_2\text{O}$  formation. These results suggest that more copper sites were occupied by sulfur species when  $\text{N}_2\text{O}$  was formed and in addition significantly less nitrates were formed in the adsorption phase, which could explain the low  $\text{N}_2\text{O}$  formation for the  $\text{SO}_3$ -exposed sample.

## 5. CONCLUSIONS

$\text{NO}_2+\text{NH}_3$  titration to form AN and subsequent temperature-programmed desorption was applied for the degreened and  $\text{SO}_2$ - and  $\text{SO}_3$ -exposed Cu-CHA to investigate the effect of  $\text{SO}_2$  and  $\text{SO}_3$  on surface nitrate and  $\text{N}_2\text{O}$  formation. Sulfation was carried out at 400 °C to mimic the scenario of  $\text{SO}_2/\text{SO}_3$  contamination of the SCR catalyst resulting from  $\text{SO}_2$  oxidation to  $\text{SO}_3/\text{H}_2\text{SO}_4$  over the DOC or coated filter.  $\text{H}_2$ -TPR and in situ DRIFTS were applied to investigate the reduction properties and surface species response in the presence of sulfur species derived by  $\text{SO}_2$ - and  $\text{SO}_3$ -exposure

treatments. Critical effects of  $\text{SO}_2$  and  $\text{SO}_3$  on Cu-CHA, its surface nitrate speciation, and  $\text{N}_2\text{O}$  formation were found. The following major findings were established:

1. First-principles calculations demonstrate that  $\text{SO}_2$  adsorption on monocopper sites results in (bi)sulfite and dicopper causes both (bi)sulfite and (bi)sulfate surface species.  $\text{SO}_3$  adsorption on mono- and dicopper results in only (bi)sulfate. Sulfur species derived from the  $\text{SO}_3$  exposure are lower in energy compared to sulfur species derived from the  $\text{SO}_2$  exposure. In addition,  $\text{SO}_x$  adsorption on the dicopper exhibits higher thermodynamic stability as compared to  $\text{SO}_x$  adsorption on the monocopper in Cu-CHA, indicating that speciation of copper has a significant effect on the speciation and thermal stability of sulfur species over Cu-CHA.
2.  $\text{SO}_3$  exposure causes a more detrimental contamination of Cu-CHA compared to  $\text{SO}_2$  exposure, according to the ICP and  $\text{H}_2$ -TPR results, in line with an earlier reported  $\text{SO}_2/\text{SO}_3$ -exposure study<sup>9</sup> as well as showing good agreement with our theoretical calculations. The  $\text{SO}_2$  exposure mainly shows sulfur contamination with  $\text{ZCuOH}$ , but the  $\text{SO}_3$  exposure results in the sulfation not only with  $\text{ZCuOH}$  but also with  $\text{Z}_2\text{Cu}$ . Therefore, the  $\text{SO}_3$ -exposed Cu-CHA shows a larger sulfur uptake compared to the  $\text{SO}_2$ -exposed Cu-CHA.
3. In situ DRIFTS demonstrated that similar surface species result from reactions between  $\text{NO}_2$  and sulfur species derived from the  $\text{SO}_2$  and  $\text{SO}_3$  exposures. After 2 min of  $\text{NO}_2$  exposure, significantly lower bands were observed in the nitrate region for the  $\text{SO}_2$ - and  $\text{SO}_3$ -exposed samples compared to the degreened sample. The results from DRIFT could explain why NO release was decreased for both  $\text{SO}_2$ - and  $\text{SO}_3$ -exposed samples during  $\text{NH}_3+\text{NO}_2$  adsorption in AN-TPD. Especially, the  $\text{SO}_3$ -exposed sample showed the lowest NO formation, suggesting that surface nitrate formation was significantly hindered due to (bi)sulfate occupying the copper sites in the form of copper-(bi)sulfate ( $\text{ZCuHSO}_4$ ).
4. AN-TPD showed similar  $\text{N}_2\text{O}$  release for the  $\text{SO}_2$ -exposed Cu-CHA compared to the degreened Cu-CHA, while a lower  $\text{NO}_2$  release for  $\text{SO}_2$ -exposed Cu-CHA. These results suggest that  $\text{SO}_2$  exposure can increase the  $\text{N}_2\text{O}$  selectivity compared to the degree end Cu-CHA during AN decomposition. In contrast,  $\text{SO}_3$ -exposed Cu-CHA shows significantly lower  $\text{N}_2\text{O}$  formation compared to the degreened and  $\text{SO}_2$ -exposed Cu-CHA, due to its highly stable sulfur species (i.e., Cu-(bi)sulfate).  $\text{SO}_3$  exposure caused more stable sulfur species compared to  $\text{SO}_2$  exposure. The stability and amount of the sulfur species are likely important factors that influence  $\text{N}_2\text{O}$  and  $\text{N}_2$  selectivity since  $\text{SO}_2$ -exposed and  $\text{SO}_3$ -exposed samples shows totally different  $\text{N}_2\text{O}$  formation properties.

## ■ ASSOCIATED CONTENT

### SI Supporting Information

The Supporting Information is available free of charge at <https://pubs.acs.org/doi/10.1021/acsengineeringau.4c00004>.

Hydrothermal synthesis of Cu-CHA and washcoating on the monolith substrate,  $\text{SO}_2$  and  $\text{SO}_3$  exposure to the Cu-CHA procedure with  $\text{SO}_3$  calibration, elemental

analysis results from ICP, N<sub>2</sub> physisorption and XRD, SEM images of zeolite crystal morphology, UV–vis DRS measurement for bulk sulfur-containing compounds, H<sub>2</sub>S detection during H<sub>2</sub>-TPR, DRIFTS, empty-tube test during the adsorption step, and SO<sub>2</sub>/H<sub>2</sub>SO<sub>4</sub>/N<sub>2</sub> release during heating in AN-TPD (PDF)

## AUTHOR INFORMATION

### Corresponding Authors

**Joonsoo Han** – Department of Chemistry and Chemical Engineering, Competence Centre for Catalysis, Chalmers University of Technology, Göteborg 41296, Sweden; Email: [joonsoo@chalmers.se](mailto:joonsoo@chalmers.se)

**Louise Olsson** – Department of Chemistry and Chemical Engineering, Competence Centre for Catalysis, Chalmers University of Technology, Göteborg 41296, Sweden; [orcid.org/0000-0002-8308-0784](https://orcid.org/0000-0002-8308-0784); Email: [louise.olsson@chalmers.se](mailto:louise.olsson@chalmers.se)

### Authors

**Joachim D. Bjerregaard** – Department of Physics and Competence Centre for Catalysis, Chalmers University of Technology, Göteborg 41296, Sweden; [orcid.org/0000-0002-3241-1467](https://orcid.org/0000-0002-3241-1467)

**Henrik Grönbeck** – Department of Physics and Competence Centre for Catalysis, Chalmers University of Technology, Göteborg 41296, Sweden; [orcid.org/0000-0002-8709-2889](https://orcid.org/0000-0002-8709-2889)

**Derek Creaser** – Department of Chemistry and Chemical Engineering, Competence Centre for Catalysis, Chalmers University of Technology, Göteborg 41296, Sweden; [orcid.org/0000-0002-5569-5706](https://orcid.org/0000-0002-5569-5706)

Complete contact information is available at:

<https://pubs.acs.org/10.1021/acseengineeringau.4c00004>

### Author Contributions

CRedit: **Joonsoo Han** conceptualization, data curation, formal analysis, investigation, methodology, writing-original draft; **Joachim Dithmer Bjerregaard** conceptualization, data curation, formal analysis, investigation, writing-original draft; **Henrik Grönbeck** conceptualization, funding acquisition, methodology, supervision, writing-review & editing; **Derek Creaser** conceptualization, methodology, supervision, writing-review & editing; **Louise Olsson** conceptualization, funding acquisition, methodology, supervision, writing-review & editing.

### Notes

The authors declare no competing financial interest.

## ACKNOWLEDGMENTS

The Competence Centre for Catalysis is hosted by Chalmers University of Technology and financially supported by the Swedish Energy Agency (Project No. 52689-1) and the member companies Johnson Matthey, Perstorp, Powercell, Preem, Scania CV, Umicore, and Volvo Group. JDB and HG acknowledge support from the European Union's Horizon 2020 research and innovation programme under the Marie Skłodowska-Curie grant agreement No. 955839 (CHASS). The calculations have been performed at PDC (Stockholm) and NSC (Linköping) through a SNIC grant.

## REFERENCES

- (1) Chen, H.-Y.; Wei, Z.; Kollar, M.; Gao, F.; Wang, Y.; Szanyi, J.; Peden, C. H. F. A comparative study of N<sub>2</sub>O formation during the selective catalytic reduction of NO<sub>x</sub> with NH<sub>3</sub> on zeolite supported Cu catalysts. *J. Catal.* **2015**, *329*, 490–498.
- (2) Gao, F.; Walter, E. D.; Kollar, M.; Wang, Y.; Szanyi, J.; Peden, C. H. F. Understanding ammonia selective catalytic reduction kinetics over Cu/SSZ-13 from motion of the Cu ions. *J. Catal.* **2014**, *319*, 1–14.
- (3) Gao, F.; Kwak, J. H.; Szanyi, J.; Peden, C. H. F. Current Understanding of Cu-Exchanged Chabazite Molecular Sieves for Use as Commercial Diesel Engine deNO<sub>x</sub> Catalysts. *Top. Catal.* **2013**, *56* (15), 1441–1459.
- (4) Shih, A. J.; González, J. M.; Khurana, I.; Ramírez, L. P.; Peña, L. A.; Kumar, A.; Villa, A. L. Influence of ZCuOH, Z<sub>2</sub>Cu, and Extraframework CuxOy Species in Cu-SSZ-13 on N<sub>2</sub>O Formation during the Selective Catalytic Reduction of NO<sub>x</sub> with NH<sub>3</sub>. *ACS Catal.* **2021**, *11* (16), 10362–10376.
- (5) Han, J.; Wang, A.; Isapour, G.; Härelind, H.; Skoglundh, M.; Creaser, D.; Olsson, L. N<sub>2</sub>O Formation during NH<sub>3</sub>-SCR over Different Zeolite Frameworks: Effect of Framework Structure, Copper Species, and Water. *Ind. Eng. Chem. Res.* **2021**, *60* (49), 17826–17839.
- (6) *Biomass—renewable energy from plants and animals*. U.S. Energy Information Administration.
- (7) Szymaszek, A.; Samojeden, B.; Motak, M. The Deactivation of Industrial SCR Catalysts—A Short Review. *Energies* **2020**, *13* (15), 3870.
- (8) Dahlin, S.; Englund, J.; Malm, H.; Feigel, M.; Westerberg, B.; Regali, F.; Skoglundh, M.; Pettersson, L. J. Effect of biofuel- and lube oil-originated sulfur and phosphorus on the performance of Cu-SSZ-13 and V<sub>2</sub>O<sub>5</sub>-WO<sub>3</sub>/TiO<sub>2</sub> SCR catalysts. *Catal. Today* **2021**, *360*, 326–339.
- (9) Hammershøi, P. S.; Jangjou, Y.; Epling, W. S.; Jensen, A. D.; Janssens, T. V. W. Reversible and irreversible deactivation of Cu-CHA NH<sub>3</sub>-SCR catalysts by SO<sub>2</sub> and SO<sub>3</sub>. *Appl. Catal. B: Environ.* **2018**, *226*, 38–45.
- (10) Xi, Y.; Ottinger, N.; Su, C.; Liu, Z. G. Sulfur Poisoning of a Cu-SSZ-13 SCR Catalyst under Simulated Diesel Engine Operating Conditions. *SAE Int. J. Adv. & Curr. Prac. in Mobility* **2021**, *3* (5), 2690–2694.
- (11) Mesilov, V. V.; Bergman, S. L.; Dahlin, S.; Xiao, Y.; Xi, S.; Zhirui, M.; Xu, L.; Chen, W.; Pettersson, L. J.; Bernasek, S. L. Differences in oxidation-reduction kinetics and mobility of Cu species in fresh and SO<sub>2</sub>-poisoned Cu-SSZ-13 catalysts. *Applied Catalysis B: Environmental* **2021**, *284*, No. 119756.
- (12) Mesilov, V.; Dahlin, S.; Bergman, S. L.; Xi, S.; Han, J.; Olsson, L.; Pettersson, L. J.; Bernasek, S. L. Regeneration of sulfur-poisoned Cu-SSZ-13 catalysts: Copper speciation and catalytic performance evaluation. *Applied Catalysis B: Environmental* **2021**, *299*, No. 120626.
- (13) Hammershøi, P. S.; Vennestrøm, P. N. R.; Falsig, H.; Jensen, A. D.; Janssens, T. V. W. Importance of the Cu oxidation state for the SO<sub>2</sub>-poisoning of a Cu-SAPO-34 catalyst in the NH<sub>3</sub>-SCR reaction. *Appl. Catal. B: Environ.* **2018**, *236*, 377–383.
- (14) Hammershøi, P. S.; Jensen, A. D.; Janssens, T. V. W. Impact of SO<sub>2</sub>-poisoning over the lifetime of a Cu-CHA catalyst for NH<sub>3</sub>-SCR. *Appl. Catal. B: Environ.* **2018**, *238*, 104–110.
- (15) Auvray, X.; Arvanitidou, M.; Högstrom, Å.; Jansson, J.; Fouladvand, S.; Olsson, L. Comparative Study of SO<sub>2</sub> and SO<sub>3</sub> Poisoning and Regeneration of Cu/BEA and Cu/SSZ-13 for NH<sub>3</sub> SCR. *Emission Control Science and Technology* **2021**, *7* (4), 232–246.
- (16) Chen, Y.-R.; Wei, L.; Kumar, A.; Wang, D.; Epling, W. S. How changes in Cu-SSZ-13 catalytic oxidation activity via mild hydrothermal aging influence sulfur poisoning extents. *Catalysis Science & Technology* **2022**, *12* (22), 6891–6902.
- (17) Cheng, Y.; Montreuil, C.; Cavataio, G.; Lambert, C. The Effects of SO<sub>2</sub> and SO<sub>3</sub> Poisoning on Cu/Zeolite SCR Catalysts. *SAE J.* **2009**.

- (18) Majewski, W. A. *Diesel Oxidation Catalyst*; DieselNet Technology Guide: DieselNet.
- (19) Kumar, A.; Li, J.; Luo, J.; Joshi, S.; Yezerets, A.; Kamasamudram, K.; Schmidt, N.; Pandya, K.; Kale, P.; Mathuraiveeran, T. *Catalyst Sulfur Poisoning and Recovery Behaviors: Key for Designing Advanced Emission Control Systems*; SAE Technical Paper Series, 2017.
- (20) Granstrand, J.; Dahlin, S.; Immele, O.; Schmalhorst, L.; Lantto, C.; Nilsson, M.; Paris, R. S.; Regali, F.; Pettersson, L. J. Catalytic aftertreatment systems for trucks fueled by biofuels – aspects on the impact of fuel quality on catalyst deactivation. In *Catalysis: Vol.30*, Vol. 30; The Royal Society of Chemistry, 2018; pp 64–145.
- (21) Majewski, W. A. *Diesel Filter Regeneration*, date of access: 2024–05–13. DieselNet Technology Guide: DieselNet.
- (22) Kumar, A.; Li, J.; Luo, J.; Joshi, S.; Yezerets, A.; Kamasamudram, K.; Schmidt, N.; Pandya, K.; Kale, P.; Mathuraiveeran, T. *Catalyst Sulfur Poisoning and Recovery Behaviors: Key for Designing Advanced Emission Control Systems*. *SAE Int.* **2017**.
- (23) Wu, Y.; Andana, T.; Wang, Y.; Chen, Y.; Walter, E. D.; Engelhard, M. H.; Rappé, K. G.; Wang, Y.; Gao, F.; Menon, U.; Daya, R.; Trandal, D.; An, H.; Zha, Y.; Kamasamudram, K.; et al. A comparative study between real-world and laboratory accelerated aging of Cu/SSZ-13 SCR catalysts. *Appl. Catal. B Environ.* **2022**, *318*, No. 121807.
- (24) Paolucci, C.; Khurana, I.; Parekh, A. A.; Li, S.; Shih, A. J.; Li, H.; Di Iorio, J. R.; Albarracin-Caballero, J. D.; Yezerets, A.; Miller, J. T.; et al. Dynamic multinuclear sites formed by mobilized copper ions in NO<sub>x</sub> selective catalytic reduction. *Science* **2017**, *357* (6354), 898–903.
- (25) Liu, C.; Malta, G.; Kubota, H.; Kon, K.; Toyao, T.; Maeno, Z.; Shimizu, K.-i. In Situ/Operando IR and Theoretical Studies on the Mechanism of NH<sub>3</sub>-SCR of NO/NO<sub>2</sub> over H-CHA Zeolites. *J. Phys. Chem. C* **2021**, *125* (25), 13889–13899.
- (26) Paolucci, C.; Parekh, A. A.; Khurana, I.; Di Iorio, J. R.; Li, H.; Albarracin Caballero, J. D.; Shih, A. J.; Anggara, T.; Delgass, W. N.; Miller, J. T.; et al. Catalysis in a Cage: Condition-Dependent Speciation and Dynamics of Exchanged Cu Cations in SSZ-13 Zeolites. *J. Am. Chem. Soc.* **2016**, *138* (18), 6028–6048.
- (27) Göttl, F.; Bhandari, S.; Lebrón-Rodríguez, E. A.; Gold, J. I.; Zones, S. I.; Hermans, I.; Dumesic, J. A.; Mavrikakis, M. Identifying hydroxylated copper dimers in SSZ-13 via UV-vis-NIR spectroscopy. *Catalysis Science & Technology* **2022**, *12* (9), 2744–2748.
- (28) Paolucci, C.; Di Iorio, J. R.; Schneider, W. F.; Gounder, R. Solvation and Mobilization of Copper Active Sites in Zeolites by Ammonia: Consequences for the Catalytic Reduction of Nitrogen Oxides. *Acc. Chem. Res.* **2020**, *53* (9), 1881–1892.
- (29) Li, H.; Paolucci, C.; Khurana, I.; Wilcox, L. N.; Göttl, F.; Albarracin-Caballero, J. D.; Shih, A. J.; Ribeiro, F. H.; Gounder, R.; Schneider, W. F. Consequences of exchange-site heterogeneity and dynamics on the UV-visible spectrum of Cu-exchanged SSZ-13. *Chem. Sci.* **2019**, *10* (8), 2373–2384.
- (30) Ipek, B.; Wulfers, M. J.; Kim, H.; Göttl, F.; Hermans, I.; Smith, J. P.; Booksh, K. S.; Brown, C. M.; Lobo, R. F. Formation of Cu<sub>2</sub>O<sub>2</sub><sup>2+</sup> and Cu<sub>2</sub>O<sup>2+</sup> toward C–H Bond Activation in Cu-SSZ-13 and Cu-SSZ-39. *ACS Catal.* **2017**, *7* (7), 4291–4303.
- (31) Wang, G.; Zhi, C.; Wang, Y.; Wang, Q. Theoretical Investigation on the Structure-Activity Relationship for Methane Activation in Cu-CHA Zeolite. *Comput. Theor. Chem.* **2023**, No. 114228.
- (32) Khurana, I.; Albarracin-Caballero, J. D.; Shih, A. J. Identification and quantification of multinuclear Cu active sites derived from monomeric Cu moieties for dry NO oxidation over Cu-SSZ-13. *J. Catal.* **2022**, *413*, 1111–1122.
- (33) Gao, F.; Mei, D.; Wang, Y.; Szanyi, J.; Peden, C. H. Selective Catalytic Reduction over Cu/SSZ-13: Linking Homo- and Heterogeneous Catalysis. *J. Am. Chem. Soc.* **2017**, *139* (13), 4935–4942.
- (34) Liu, B.; Yao, D.; Wu, F.; Wei, L.; Li, X.; Wang, X. Experimental Investigation on N<sub>2</sub>O Formation during the Selective Catalytic Reduction of NO<sub>x</sub> with NH<sub>3</sub> over Cu-SSZ-13. *Ind. Eng. Chem. Res.* **2019**, *58* (45), 20516–20527.
- (35) Xi, Y.; Ottinger, N. A.; Keturakis, C. J.; Liu, Z. G. Dynamics of low temperature N<sub>2</sub>O formation under SCR reaction conditions over a Cu-SSZ-13 catalyst. *Appl. Catal. B: Environ.* **2021**, *294*, No. 120245.
- (36) Feng, Y.; Janssens, T. V. W.; Vennestrom, P. N. R.; Jansson, J.; Skoglundh, M.; Grönbeck, H. The Role of H<sup>+</sup>- and Cu<sup>+</sup>-Sites for N<sub>2</sub>O Formation during NH<sub>3</sub>-SCR over Cu-CHA. *J. Phys. Chem. C* **2021**, *125* (8), 4595–4601.
- (37) Shih, A. J.; González, J. M.; Khurana, I.; Ramirez, L. P.; Peña, L. A.; Kumar, A.; Villa, A. L. Influence of ZCuOH, Z<sub>2</sub>Cu, and Extraframework CuO<sub>y</sub> Species in Cu-SSZ-13 on N<sub>2</sub>O Formation during the Selective Catalytic Reduction of NO<sub>x</sub> with NH<sub>3</sub>. *ACS Catal.* **2021**, *0* (0), 10362–10376.
- (38) Gao, F.; Peden, C. H. F. Recent Progress in Atomic-Level Understanding of Cu/SSZ-13 Selective Catalytic Reduction Catalysts. *Catalysts* **2018**, *8* (4), 140.
- (39) Shan, Y.; He, G.; Du, J.; Sun, Y.; Liu, Z.; Fu, Y.; Liu, F.; Shi, X.; Yu, Y.; He, H. Strikingly distinctive NH<sub>3</sub>-SCR behavior over Cu-SSZ-13 in the presence of NO<sub>2</sub>. *Nat. Commun.* **2022**, *13* (1), 4606.
- (40) Kubota, H.; Liu, C.; Toyao, T.; Maeno, Z.; Ogura, M.; Nakazawa, N.; Inagaki, S.; Kubota, Y.; Shimizu, K.-i. Formation and Reactions of NH<sub>4</sub>NO<sub>3</sub> during Transient and Steady-State NH<sub>3</sub>-SCR of NO<sub>x</sub> over H-AFX Zeolites: Spectroscopic and Theoretical Studies. *ACS Catal.* **2020**, *10* (3), 2334–2344.
- (41) Liu, C.; Malta, G.; Kubota, H.; Toyao, T.; Maeno, Z.; Shimizu, K.-i. Mechanism of NH<sub>3</sub>-Selective Catalytic Reduction (SCR) of NO/NO<sub>2</sub> (Fast SCR) over Cu-CHA Zeolites Studied by In Situ/Operando Infrared Spectroscopy and Density Functional Theory. *J. Phys. Chem. C* **2021**, *125* (40), 21975–21987.
- (42) Chen, L.; Janssens, T. V. W.; Vennestrom, P. N. R.; Jansson, J.; Skoglundh, M.; Grönbeck, H. A Complete Multisite Reaction Mechanism for Low-Temperature NH<sub>3</sub>-SCR over Cu-CHA. *ACS Catal.* **2020**, *10* (10), 5646–5656.
- (43) Kumar, A.; Kamasamudram, K.; Currier, N.; Yezerets, A. Effect of Transition Metal Ion Properties on the Catalytic Functions and Sulfation Behavior of Zeolite-Based SCR Catalysts. *SAE International Journal of Engines* **2017**, *10* (4), 1604–1612.
- (44) Jangjou, Y.; Ali, M.; Chang, Q.; Wang, D.; Li, J.; Kumar, A.; Epling, W. S. Effect of SO<sub>2</sub> on NH<sub>3</sub> oxidation over a Cu-SAPO-34 SCR catalyst. *Catalysis Science & Technology* **2016**, *6* (8), 2679–2685.
- (45) Jangjou, Y.; Do, Q.; Gu, Y.; Lim, L.-G.; Sun, H.; Wang, D.; Kumar, A.; Li, J.; Grabow, L. C.; Epling, W. S. Nature of Cu Active Centers in Cu-SSZ-13 and Their Responses to SO<sub>2</sub> Exposure. *ACS Catal.* **2018**, *8* (2), 1325–1337.
- (46) Shih, A. J.; Khurana, I.; Li, H.; González, J.; Kumar, A.; Paolucci, C.; Lardinois, T. M.; Jones, C. B.; Albarracin Caballero, J. D.; Kamasamudram, K.; Yezerets, A.; Delgass, W. N.; Miller, J. T.; Villa, A. L.; Schneider, W. F.; Gounder, R.; Ribeiro, F. H.; et al. Spectroscopic and kinetic responses of Cu-SSZ-13 to SO<sub>2</sub> exposure and implications for NO<sub>x</sub> selective catalytic reduction. *Appl. Catal. A: Gen.* **2019**, *574*, 122–131.
- (47) Jangjou, Y.; Wang, D.; Kumar, A.; Li, J.; Epling, W. S. SO<sub>2</sub> Poisoning of the NH<sub>3</sub>-SCR Reaction over Cu-SAPO-34: Effect of Ammonium Sulfate versus Other S-Containing Species. *ACS Catal.* **2016**, *6* (10), 6612–6622.
- (48) Wang, A.; Olsson, L. Insight into the SO<sub>2</sub> poisoning mechanism for NO<sub>x</sub> removal by NH<sub>3</sub>-SCR over Cu/LTA and Cu/SSZ-13. *Chemical Engineering Journal* **2020**, *395*, 125048.
- (49) Wijayanti, K.; Xie, K.; Kumar, A.; Kamasamudram, K.; Olsson, L. Effect of gas compositions on SO<sub>2</sub> poisoning over Cu/SSZ-13 used for NH<sub>3</sub>-SCR. *Applied Catalysis B: Environmental* **2017**, *219*, 142–154.
- (50) Su, W.; Li, Z.; Zhang, Y.; Meng, C.; Li, J. Identification of sulfate species and their influence on SCR performance of Cu/CHA catalyst. *Catalysis Science & Technology* **2017**, *7* (7), 1523–1528.



- (51) Zhang, Y.; Zhu, H.; Zhang, T.; Li, J.; Chen, J.; Peng, Y.; Li, J. Revealing the Synergistic Deactivation Mechanism of Hydrothermal Aging and SO<sub>2</sub> Poisoning on Cu/SSZ-13 under SCR Condition. *Environ. Sci. Technol.* **2022**, *56* (3), 1917–1926.
- (52) Shih, A. J.; Khurana, I.; Li, H.; González, J.; Kumar, A.; Paolucci, C.; Lardinois, T. M.; Jones, C. B.; Albarracín Caballero, J. D.; Kamasamudram, K.; et al. Spectroscopic and kinetic responses of Cu-SSZ-13 to SO<sub>2</sub> exposure and implications for NO<sub>x</sub> selective catalytic reduction. *Applied Catalysis A: General* **2019**, *574*, 122–131.
- (53) Luo, J.; Wang, D.; Kumar, A.; Li, J.; Kamasamudram, K.; Currier, N.; Yezerets, A. Identification of two types of Cu sites in Cu/SSZ-13 and their unique responses to hydrothermal aging and sulfur poisoning. *Catal. Today* **2016**, *267*, 3–9.
- (54) Hammershøi, P. S.; Godiksen, A. L.; Mossin, S.; Vennestrom, P. N. R.; Jensen, A. D.; Janssens, T. V. W. Site selective adsorption and relocation of SO<sub>x</sub> in deactivation of Cu-CHA catalysts for NH<sub>3</sub>-SCR. *React. Chem. Eng.* **2019**, *4* (6), 1081–1089.
- (55) Molokova, A. Y.; Borfecchia, E.; Martini, A.; Pankin, I. A.; Atzori, C.; Mathon, O.; Bordiga, S.; Wen, F.; Vennestrom, P. N. R.; Berlier, G.; et al. SO<sub>2</sub> Poisoning of Cu-CHA deNO<sub>x</sub> Catalyst: The Most Vulnerable Cu Species Identified by X-ray Absorption Spectroscopy. *JACS Au* **2022**, *0* (0), 787.
- (56) Cheng, Y.; Lambert, C.; Kim, D. H.; Kwak, J. H.; Cho, S. J.; Peden, C. H. F. The different impacts of SO<sub>2</sub> and SO<sub>3</sub> on Cu/zeolite SCR catalysts. *Catal. Today* **2010**, *151* (3–4), 266–270.
- (57) Bjerregaard, J. D.; Votsmeier, M.; Grönbeck, H. Mechanism for SO<sub>2</sub> poisoning of Cu-CHA during low temperature NH<sub>3</sub>-SCR. *J. Catal.* **2023**, *417*, 497–506.
- (58) Wijayanti, K.; Leistner, K.; Chand, S.; Kumar, A.; Kamasamudram, K.; Currier, N. W.; Yezerets, A.; Olsson, L. Deactivation of Cu-SSZ-13 by SO<sub>2</sub> exposure under SCR conditions. *Catalysis Science & Technology* **2016**, *6* (8), 2565–2579.
- (59) Bergman, S. L.; Dahlin, S.; Mesilov, V. V.; Xiao, Y.; Englund, J.; Xi, S.; Tang, C.; Skoglundh, M.; Pettersson, L. J.; Bernasek, S. L. In-situ studies of oxidation/reduction of copper in Cu-CHA SCR catalysts: Comparison of fresh and SO<sub>2</sub>-poisoned catalysts. *Applied Catalysis B: Environmental* **2020**, *269*, No. 118722.
- (60) Bergman, S. L.; Dahlin, S.; Mesilov, V. V.; Xiao, Y.; Englund, J.; Xi, S.; Tang, C.; Skoglundh, M.; Pettersson, L. J.; Bernasek, S. L. In-situ studies of oxidation/reduction of copper in Cu-CHA SCR catalysts: Comparison of fresh and SO<sub>2</sub>-poisoned catalysts. *Applied Catalysis B: Environmental* **2020**, *269*, 118722.
- (61) Kresse, G.; Furthmüller, J. Efficient iterative schemes for ab initio total-energy calculations using a plane-wave basis set. *Phys. Rev. B Condens Matter* **1996**, *54* (16), 11169–11186. From NLM
- (62) Kresse, G.; Hafner, J. Ab initio molecular-dynamics simulation of the liquid-metal–amorphous-semiconductor transition in germanium. *Phys. Rev. B* **1994**, *49* (20), 14251–14269.
- (63) Blöchl, P. E. Projector augmented-wave method. *Phys. Rev. B* **1994**, *50* (24), 17953–17979.
- (64) Kresse, G.; Joubert, D. From ultrasoft pseudopotentials to the projector augmented-wave method. *Phys. Rev. B* **1999**, *59* (3), 1758–1775.
- (65) Perdew, J. P.; Burke, K.; Ernzerhof, M. Generalized Gradient Approximation Made Simple. *Phys. Rev. Lett.* **1996**, *77* (18), 3865–3868. From NLM
- (66) Grimme, S.; Antony, J.; Ehrlich, S.; Krieg, H. A consistent and accurate ab initio parametrization of density functional dispersion correction (DFT-D) for the 94 elements H–Pu. *J. Chem. Phys.* **2010**, *132* (15), No. 154104. From NLM
- (67) Mills, G.; Jónsson, H.; Schenter, G. K. Reversible work transition state theory: application to dissociative adsorption of hydrogen. *Surf. Sci.* **1995**, *324* (2), 305–337.
- (68) Henkelman, G.; Jónsson, H. Improved tangent estimate in the nudged elastic band method for finding minimum energy paths and saddle points. *J. Chem. Phys.* **2000**, *113* (22), 9978–9985.
- (69) Nosé, S. A unified formulation of the constant temperature molecular dynamics methods. *J. Chem. Phys.* **1984**, *81* (1), 511–519.
- (70) Hoover, W. G. Canonical dynamics: Equilibrium phase-space distributions. *Phys. Rev. A Gen Phys.* **1985**, *31* (3), 1695–1697. From NLM
- (71) Tang, W.; Sanville, E.; Henkelman, G. A grid-based Bader analysis algorithm without lattice bias. *J. Phys.: Condens. Matter* **2009**, *21* (8), No. 084204.
- (72) Yu, M.; Trinkle, D. R. Accurate and efficient algorithm for Bader charge integration. *J. Chem. Phys.* **2011**, *134* (6), No. 064111.
- (73) Hun Kwak, J.; Zhu, H.; Lee, J. H.; Peden, C. H. F.; Szanyi, J. Two different cationic positions in Cu-SSZ-13? *Chem. Commun.* **2012**, *48* (39), 4758–4760.
- (74) Wang, X.; Chen, L.; Vennestrom, P. N. R.; Janssens, T. V. W.; Jansson, J.; Grönbeck, H.; Skoglundh, M. Direct measurement of enthalpy and entropy changes in NH<sub>3</sub> promoted O<sub>2</sub> activation over Cu-CHA at low temperature. *ChemCatChem* **2021**, *n/a* (n/a), 2577.
- (75) Rhoda, H. M.; Plessers, D.; Heyer, A. J.; Bols, M. L.; Schoonheydt, R. A.; Sels, B. F.; Solomon, E. I. Spectroscopic Definition of a Highly Reactive Site in Cu-CHA for Selective Methane Oxidation: Tuning a Mono- $\mu$ -Oxo dicopper(II) Active Site for Reactivity. *J. Am. Chem. Soc.* **2021**, *143* (19), 7531–7540. note = PMID: 33970624
- (76) Bregante, D. T.; Wilcox, L. N.; Liu, C.; Paolucci, C.; Gounder, R.; Flaherty, D. W. Dioxygen Activation Kinetics over Distinct Cu Site Types in Cu-chabazite Zeolites. *ACS Catal.* **2021**, *11* (19), 11873–11884.
- (77) Mesilov, V.; Xiao, Y.; Dahlin, S.; Bergman, S. L.; Pettersson, L. J.; Bernasek, S. L. First-Principles Calculations of Condition-Dependent Cu/Fe Speciation in Sulfur-Poisoned Cu- and Fe-SSZ-13 Catalysts. *J. Phys. Chem. C* **2021**, *125* (8), 4632–4645.
- (78) Mesilov, V.; Dahlin, S.; Bergman, S. L.; Hammershøi, P. S.; Xi, S.; Pettersson, L. J.; Bernasek, S. L. Insights into sulfur poisoning and regeneration of Cu-SSZ-13 catalysts: in situ Cu and S K-edge XAS studies. *Catal. Sci. Technol.* **2021**, *11* (16), 5619–5632.
- (79) Waseda, Y.; Matsubara, E.; Shinoda, K. *X-Ray Diffraction Crystallography*; Springer Berlin: Heidelberg, 2011. DOI: 10.1007/978-3-642-16635-8.
- (80) Giordanino, F.; Vennestrom, P. N.; Lundegaard, L. F.; Stappen, F. N.; Mossin, S.; Beato, P.; Bordiga, S.; Lamberti, C. Characterization of Cu-exchanged SSZ-13: a comparative FTIR, UV-Vis, and EPR study with Cu-ZSM-5 and Cu-beta with similar Si/Al and Cu/Al ratios. *Dalton Trans* **2013**, *42* (35), 12741–12761.
- (81) Korhonen, S. T.; Fickel, D. W.; Lobo, R. F.; Weckhuysen, B. M.; Beale, A. M. Isolated Cu<sup>2+</sup> ions: active sites for selective catalytic reduction of NO. *Chem. Commun. (Camb)* **2011**, *47* (2), 800–802.
- (82) Gao, F.; Washton, N. M.; Wang, Y.; Kollár, M.; Szanyi, J.; Peden, C. H. F. Effects of Si/Al ratio on Cu/SSZ-13 NH<sub>3</sub>-SCR catalysts: Implications for the active Cu species and the roles of Brønsted acidity. *J. Catal.* **2015**, *331*, 25–38.
- (83) Gao, F.; Kwak, J. H.; Szanyi, J.; Peden, C. H. F. Current Understanding of Cu-Exchanged chabazite Molecular Sieves for Use as Commercial Diesel Engine deNO<sub>x</sub> Catalysts. *Top. Catal.* **2013**, *56* (15–17), 1441–1459.
- (84) Bjerregaard, J. D.; Han, J.; Creaser, D.; Olsson, L.; Grönbeck, H. On the Interpretation of H<sub>2</sub>-TPR from Cu-CHA using First-Principles Calculations. *J. Phys. Chem. C* **2023**, 4525.
- (85) Wang, A.; Olsson, L. Insight into the SO<sub>2</sub> poisoning mechanism for NO<sub>x</sub> removal by NH<sub>3</sub>-SCR over Cu/LTA and Cu/SSZ-13. *Chemical Engineering Journal* **2020**, *395*, No. 125048.
- (86) Dahlin, S.; Lantto, C.; Englund, J.; Westerberg, B.; Regali, F.; Skoglundh, M.; Pettersson, L. J. Chemical aging of Cu-SSZ-13 SCR catalysts for heavy-duty vehicles – Influence of sulfur dioxide. *Catal. Today* **2019**, *320*, 72–83.
- (87) Colombo, M.; Nova, I.; Tronconi, E. A comparative study of the NH<sub>3</sub>-SCR reactions over a Cu-zeolite and a Fe-zeolite catalyst. *Catal. Today* **2010**, *151* (3–4), 223–230.
- (88) Villamaina, R.; Liu, S.; Nova, I.; Tronconi, E.; Ruggeri, M. P.; Collier, J.; York, A.; Thompsett, D. Speciation of Cu Cations in Cu-CHA Catalysts for NH<sub>3</sub>-SCR: Effects of SiO<sub>2</sub>/AlO<sub>3</sub> Ratio and Cu

Loading Investigated by Transient Response Methods. *ACS Catal.* **2019**, *9* (10), 8916–8927.

(89) Ruggeri, M. P.; Nova, I.; Tronconi, E.; Pihl, J. A.; Toops, T. J.; Partridge, W. P. In-situ DRIFTS measurements for the mechanistic study of NO oxidation over a commercial Cu-CHA catalyst. *Applied Catalysis B: Environmental* **2015**, *166–167*, 181–192.

(90) Park, J.; Lin, M. C. Thermal Decomposition of Gaseous Ammonium Nitrate at Low Pressure: Kinetic Modeling of Product Formation and Heterogeneous Decomposition of Nitric Acid. *J. Phys. Chem. A* **2009**, *113* (48), 13556–13561. note = PMID: 19845384

(91) Negri, C.; Hammershoi, P. S.; Janssens, T. V. W.; Beato, P.; Berlier, G.; Bordiga, S. Investigating the Low Temperature Formation of Cu(II) -(N,O) Species on Cu-CHA Zeolites for the Selective Catalytic Reduction of NOx. *Chemistry* **2018**, *24* (46), 12044–12053.

(92) Negri, C.; Borfecchia, E.; Cutini, M.; Lomachenko, K. A.; Janssens, T. V. W.; Berlier, G.; Bordiga, S. Evidence of Mixed-Ligand Complexes in Cu-CHA by Reaction of Cu Nitrates with NO/NH<sub>3</sub> at Low Temperature. *ChemCatChem*. **2019**, *11* (16), 3828–3838.

(93) Chen, H.-Y.; Wei, Z.; Kollar, M.; Gao, F.; Wang, Y.; Szanyi, J.; Peden, C. H. F. NO oxidation on zeolite supported Cu catalysts: Formation and reactivity of surface nitrates. *Catal. Today* **2016**, *267*, 17–27.

(94) Bordiga, S.; Regli, L.; Lamberti, C.; Zecchina, A.; Bjørgen, M.; Lillerud, K. P. FTIR Adsorption Studies of H<sub>2</sub>O and CH<sub>3</sub>OH in the Isostructural H-SSZ-13 and H-SAPO-34: Formation of H-Bonded Adducts and Protonated Clusters. *J. Phys. Chem. B* **2005**, *109* (16), 7724–7732. note = PMID: 16851897

(95) Zhang, R.; McEwen, J.-S.; Kollár, M.; Gao, F.; Wang, Y.; Szanyi, J.; Peden, C. H. F. NO Chemisorption on Cu/SSZ-13: A Comparative Study from Infrared Spectroscopy and DFT Calculations. *ACS Catal.* **2014**, *4* (11), 4093–4105.

(96) Negri, C.; Martini, A.; Deplano, G.; Lomachenko, K. A.; Janssens, T. V. W.; Borfecchia, E.; Berlier, G.; Bordiga, S. Investigating the role of Cu-oxo species in Cu-nitrate formation over Cu-CHA catalysts. *Phys. Chem. Chem. Phys.* **2021**, 18322.

(97) Grossale, A.; Nova, I.; Tronconi, E.; Chatterjee, D.; Weibel, M. The chemistry of the NO/NO<sub>2</sub>-NH<sub>3</sub> “fast” SCR reaction over Fe-ZSMS investigated by transient reaction analysis. *J. Catal.* **2008**, *256* (2), 312–322.

(98) Colombo, M.; Nova, I.; Tronconi, E. Detailed kinetic modeling of the NH<sub>3</sub>-NO/NO<sub>2</sub> SCR reactions over a commercial Cu-zeolite catalyst for Diesel exhausts after treatment. *Catal. Today* **2012**, *197* (1), 243–255.

(99) Lee, S.; Nimlos, C. T.; Kipp, E. R.; Wang, Y.; Gao, X.; Schneider, W. F.; Lusardi, M.; Vattipalli, V.; Prasad, S.; Moini, A.; et al. Evolution of Framework Al Arrangements in CHA Zeolites during Crystallization in the Presence of Organic and Inorganic Structure-Directing Agents. *Cryst. Growth Des.* **2022**, *22*, 6275.

(100) Cui, Y.; Gao, F. Cu Loading Dependence of Fast NH<sub>3</sub>-SCR on Cu/SSZ-13. *Emission Control Science and Technology* **2019**, *5* (2), 124–132.